2012-10-01

Polarimetric Synthetic Aperture Radar Measurements of Snow Covered First-Year Sea Ice

Hossain, Md. Mosharraf

UNIVERSITY OF CALGARY

Polarimetric Synthetic Aperture Radar Measurements of Snow Covered First-Year Sea Ice

by

Md. Mosharraf Hossain

A THESIS

SUBMITTED TO THE FACULTY OF GRADUATE STUDIES IN PARTIAL FULFILLMENT

OF THE REQUIREMENTS FOR THE DEGREE OF

MASTER OF SCIENCE

DEPARTMENT OF GEOGRAPHY

CALGARY, ALBERTA

SEPTEMBER, 2012

Abstract

This study examines the utility of fully polarimetric C-and SAR parameters and three-component scattering model to quantify the sensitivity of snow covered first-year sea ice (FYI) to radar incidence angles and surface air temperature (SAT) during the late winter transition. This three-component scattering model is based on surface, double-bounce and volume scattering contributed from various materials and surface properties. RADARSAT-2 C-band fully polarimetric synthetic aperture radar (POLSAR) data is utilized to quantify the sensitivity of thermodynamic effects ($-8° \, C$ and $-0.4° \, C$) of the polarimetric backscatter signature on mean snow cover thickness ranging from 8 cm to 36 cm with in-situ geophysical data from four different validation sites along with two different radar incidence angles 29° (steep) and 39° (shallow) to discriminate between snow-covered smooth, rough and deformed FYI. The result shows enhanced discrimination at shallower incidence angles compared to steeper ones in both 2-D and 3-D plots. The double-bounce scattering contribution is low for all FYI types at both incidence angles which are attributed to shallower incidence angle as microwave energy being in direct contact with a greater volume of higher dielectric brine coated, enlarged snow grains in the basal layer compared to the steeper incidence angles. The results also show that surface scattering dominates for all three FYI types at both incidence angles and decreases with increasing surface roughness and radar incidence angles whereas opposite results observed for volume scattering mechanisms. The results indicate that higher variation measured for thin snow class $\sim 7 \, dB$ for both co- cross-polarization backscatters compared to thick snow class $\sim 1 \, dB$ which corroborates with electro-thermodynamic theory.

Key words: Three-component scattering model, Snow cover, First-year sea ice, synthetic aperture radar.

ACKNOWLEDGEMENTS

At first I would like to express my gratefulness to the Almighty because without his blessings it was not possible to complete this work. Then, I would like to thank my supervisor Dr. John J. Yackel for his invaluable guidance, support, and intellectual insight. It has been a pleasure to work with you over the last couple of years. Thanks also to committee member Dr. Ayman F. Habib (Geomatics Engineering) and Dr. Mryka Hall-Beyer (Geography) for their valuable input. I would like to express my sincere gratitude to Dr. Mohammed Dabboor, Dr. Torsten Geldsetzer, and Dr. Yi-Ching Chung for their guidance in data processing, analysis and particularly various technical aspects of my thesis. Thank you for inspiring to carry out sea ice research.

Thank you to my colleagues who graciously gave their time and helped me by providing collaboration and assistance with my research. In particular I thank Dr. Randy Scharien, Chris M. Fuller, J.V. Gill, Melissa Peters, Peter Bezeau, Sanjiv Gautam, Dr. Surendra Adhikari, Johnson Chan, Adrienne Cunnings and Md. Raied Hasan.

I would like to thank Bart Hulshof for his affable help during my satellite data analysis.

Another group of individuals that needs to be acknowledged are those that provided data and equipment for my thesis. I would like to thank Environment Canada, Canadian Ice Service for their meteorological data, Canadian Space Agency SOAR-E for RADARSAT-2 images, and PCI Geomatica, RAT and ENVI for software support.

I wish to express my sincere thanks to all my friends in Calgary and outside whose advice and assistance aided considerably to the completion of this thesis. You know who you are. The emotional and mental support has not gone unnoticed. Without you, I don't know where I would be.

Lastly, I would like to deeply and sincerely thank my family, especially my father (Md. Altaf Hossain) and departed soul of my mother for their help and encouragement to me to undertake graduate studies and for their endless support throughout my academic endeavours.

Md. Mosharraf Hossain

September, 2012

DEDICATION

This thesis is dedicated to departed soul of my beloved mother (Late Mrs. Alia Begum), and grandparents- (Late Md. Mohasin Ali Miah and Late Mrs. Rizia Khatun).

TABLE OF CONTENTS

List of Tables

List of Figures

LIST OF SYMBOLS AND ABBREVIATIONS

Commonly referenced symbols:

α	Alpha Angle
H_1	Alternative Hypothesis
A	Anisotropy
σ^0	Area-extensive Scattering Coefficient
σ_{xy}^0	Cross-polarization (HV)
γ_{co}	Co-polarized Ratio
γ_{cr}	Cross-polarized Ratio
φ_{xx-yy}	Co-polarized Phase Difference
μ_{xxyy}	Complex Co-polarized Correlation Coefficient
P_d	Double-Bounce Scattering
H	Entropy
f	Frequency
F_p	Fractional Polarization
σ_{xx}^0	Horizontal Co-polarization (HH)
θ	Incidence Angle
H_0	Null Hypothesis
δ_p	Penetration Depth
P	Pedestal Height
σ^0	Radar Scattering Cross Section
RGB	Red, Green and Blue

P_s	Surface Scattering
T_p	Total Power/SPAN
σ^0_{yy}	Vertical Co-polarization (VV)
P_v	Volume Scattering
λ	Wavelength

Commonly referenced abbreviations:

AIRSAR	Airborne Synthetic Aperture Radar
ANOVA	Analysis of Variance
°C	Degree Celsius
CFL	Circumpolar Flaw Lead System Study
CIS	Canadian Ice Service
dB	Decibel
DI	Deformed Ice
EC	Environment Canada
EM	Electromagnetic
EMR	Electromagnetic Radiation
ENL	Equivalent Number of Looks
FYI	First-Year Sea Ice
GCM	General Circulation Model
GHz	Gigahertz
GPS	Global Positioning System
GTP	Ground Truth Point
IST	Ice Surface Temperature
IPCC	Intergovernmental Panel on Climate Change
IPY	International Polar Year
LWC	Liquid Water Content

MSC	MANICE (Manual of Standard Procedures for Observing and Reporting Ice Conditions)
MYI	Multi-Year Sea Ice
NESZ	Noise-Equivalent Sigma-Zero
NWT	Northwest Territories
OSA	Ocean Sea-Ice Atmosphere
PAR	Photosynthetically Active Radiation
Pol	Polarization (prefixed by single-, dual-, quad-, co- or cross-)
POLSAR	Polarimetric Synthetic Aperture Radar
PSU	Practical Salinity Units
RI	Rough Ice
ROI	Region of Interest
RSAT-2	RADARSAT-2
SAR	Synthetic Aperture Radar
SCA	Snow Covered Area
SI	Smooth Ice
SYI	Second Year Ice
SWE	Snow Water Equivalent
UTC	Coordinated Universal Time
WMO	World Meteorological Organization
WS	Weather Research Station
YD	Year Day

CONTRIBUTIONS OF AUTHORS

This dissertation consists of a series of manuscripts that have been submitted to academic journals. As such there is some repetition between these chapters regarding study site and methods, however, all results are unique. The text from each manuscript is reprinted largely as it appears in the journals for publication, but with minor changes to some of the language, which were made to make this dissertation a more cohesive document. Additional changes to the reference style and figures have also been made to ensure consistency with the dissertation format. While all of these papers are co-authored, I am the lead author on all of the studies and am responsible for all statistical analysis and modelling work appearing in them. All manuscript figures are reproduced with permission from the copyright holders.

Chapter 4 has been submitted to the International Journal of Remote Sensing.

Hossain, M.M., Yackel, J.J., and Dabboor, M. (Submitted, May 28, 2012). Application of a three-component scattering model over snow-covered first-year sea ice using polarimetric C-band SAR data. *International Journal of Remote Sensing*. Pg. 1-35. Reference # TRES-PAP-2012-0379.

Chapter 5 is in submission to the journal of *IEEE Transactions on Geoscience and Remote Sensing*

Hossain, M.M., Yackel, J.J., and Geldsetzer, T. (*In-preparation*). Observations of snow water equivalent on landfast smooth first-year sea ice during late winter by using polarimetric C-band SAR data. *IEEE Transactions on Geoscience and Remote Sensing.* Sub #: TGRS-2012-000X.

For all publications, MMH designed the research, finalized the output results, and led the writing of the manuscript and revisions. Other co-authors provided feedback in organization, discussion and interpretation of results and contributed to the writing.

Chapter One

INTRODUCTION

1.1 Study Context

The Arctic is an important region to hemispheric and global scale climate processes (Intergovernmental Panel on Climate Change, IPCC, 1996) and the role of ocean-sea ice-atmosphere (OSA) interactions is actively being assessed. Variability of sea ice types, extent and composition impacts Arctic biodiversity, cultural, economic and global climate systems. Consideration of our polar climates, and in particular, the marine cryosphere, within global climate modeling efforts is paramount due to the enhanced sensitivity of these regions to environmental perturbations. Snow covered sea ice makes up the majority of the marine cryosphere. The sensitivity exists because the effect of snow covered sea ice is far out of proportion to its geographical area (Carmack, 1986). The sensitivity arises due to a number of feedback processes operating between the cryosphere, ocean and atmosphere, which may contribute to the amplification of any natural or anthropogenic perturbation (LeDrew, 1986). The properties of snow and ice, i.e. thermal conductivity, diffusivity, reflection, absorption and transmission determine energy transfer among the OSA (Mortiz and Perovich, 1996; Kotlyakov and Grosswald, 1990). The snow cover acts as a barrier between the cold atmosphere and the relatively warm ocean, hampering energy transfer and controlling sea ice growth. During the freeze-up and spring melt transition, snow cover modulates the sea ice growth and decay through reduction and moderation of incoming short-wave radiation entering into the ice layer (Maykut, 1986; Eicken et al., 1995; Eicken, 2003).

The spatial and temporal variability of the snow cover on sea ice also controls the geophysical processes operating across the OSA interface. These controls can range from micro

to meso scales influencing regional ecology and the global climate system. At the micro scale, the penetration of photosynthetically active radiation (PAR) through the snow cover determines growth of epontic algal communities in the marine ecosystem whereby snow which is too thick or too thin hinders the algal growth by either too little or too much PAR, thus reducing the primary producer in the food cycle (Iacozza and Barber, 1999). This can have significant implications on the Arctic ecosystem. At local to regional scales, snow cover controls the life cycle of arctic ringed seal and polar bear (Kinnard et al., 2011; Strling and Smith, 2004; Ferguson et al., 2005). Thick snow on ridged sea ice provides protection for the *ringed seal* from predators and cold atmospheric conditions (Frost et al., 1988; Furgal et al., 1996) whereas it also hampers polar bear movement and hunting (Striling et al., 1993). At global scales, the Arctic is already exhibiting signs of global climate change compared to temperate or tropical regions due to polar amplification (Monaghan and Bromwich, 2008; Serreze et al., 2009; Budikova, 2009). Since snow cover dominates the energy balance of the OSA due to its low thermal diffusivity and high albedo, it plays a vital role in the global climate system. Seasonal or first-year sea ice is becoming a much more prevalent ice type in the Arctic as a result of significant multi-year sea ice losses in recent years (Maslanik et al., 2011). This makes studies of seasonal ice increasingly important.

Snow cover on landfast first-year sea ice (FYI) in the Canadian Arctic during the late winter and early spring is usually shallow (mean is ~ 20 cm) but highly variable, ranging from 0 to 75 cm (Iacozza and Barber, 1999; 2001; Sturm et al., 2002; 2006; Yackel et al., 2007). The snow thickness is largely a function of sea ice type, ice surface roughness and regional meteorological history following freeze-up which can be modeled statistically with moderate success (Iacozza and Barber, 1999). Passive microwave remote sensing techniques are available

to measure snow thickness on sea ice but are at scales which approach tens to hundreds of kilometers (Markus and Cavalieri, 1998). Estimation of snow thickness at these scales is not suitable for high resolution thermodynamic models (Hanesiak et al., 1999) or for calculating photosynthetically active radiation (PAR) penetration into ocean water through snow cover (Iacozza and Barber, 1999). The spatial distribution of snow cover (or snow thickness distribution) and/or snow water equivalent (SWE) on FYI is largely determined by the amount of meteoric snowfall over the region and by the magnitude of wind speed and direction during snow depositional and redistribution events (Iacozza and Barber, 2001; 2010; Strum et al., 2002; Petrich et al., 2012).

In-situ geophysical measurement of snow thickness on FYI in the Canadian Archipelago is expensive and time consuming. As a result, our ability to achieve first-order estimates of SWE is extremely restricted due to the sparse number of snow measurement stations and historical datasets. Previous research has demonstrated that snow thickness (or SWE) and/or meteoric snowfall measurements from shore-based stations are not accurately representative of SWE or snowfall over adjacent sea ice (Hanesiak et al., 1999). This can be due to the local cyclonic activity, wind fetch, catchment, etc, of landmasses. These limitations encourage development of a remote sensing and/or modeling approach for estimation of snow thickness distribution on FYI.

Active microwave remote sensing, with both space and ground based sensors, has been extensively used by both the scientific and operational communities to characterize and quantify the spatio-temporal variability of FYI types that routinely co-exist within polar waters. Single channel and single linear polarization synthetic aperture radar (SAR) data have been used for sea ice analysis since October 10, 1978 beginning with SeaSAT (Swift, 1999). More recently, multi-frequency, multi-polarized SAR data has been explored to exploit snow covered sea ice physical

properties. The majority of these works have been concentrated on sea ice classification (e.g. Carlström and Ulander, 1995; Dierking and Askine, 1998; Dabboor et al., 2012; Karvonen, et al., 2003; Simila et al., 2006; Geldsetzer and Yackel, 2009). Most of the sea ice research has been conducted using single and dual co-polarized signatures to retrieve sea ice geophysical information, as several researchers have found that single polarized backscatter coefficient signatures are not sufficient to discriminate FYI types (van der Sanden, 2004; Geldsetzer and Yackel, 2009) and estimate sea ice concentration (van der Sanden, 2004). Dual and multi-polarized backscatter coefficients are potentially useful for sea ice classification and interpretation (Dierking and Askine, 1998; Dierking, 2010). Fully polarimetric synthetic aperture radar (POLSAR) data employing magnitude and phase information provides additional information which may resolve some of these ambiguities (van der Sanden, 2004; Scheulch et al., 2005; Dierking, 2010). Co- and cross-polarized backscatter ratios provide significant discrimination between different ice types and open water (Geldsetzer and Yackel, 2009).

Numerous studies (Barber and Nghiem, 1999; Barber et al., 1998a; Tjuatja et al., 1995) have evaluated the microwave scattering and emission properties of snow covered sea ice because of the unique ability of microwaves to provide measurements of the surface irrespective of cloud cover or daylight. Microwave scattering properties of snow covered sea ice have been investigated by Beaven et al., 1995; Lytle et al., 1993; Bredow and Gogineni, 1990. The geophysical and thermodynamic properties of snow covered sea ice have been evaluated by Yackel and Barber, (2007) and Barber and Nghiem (1999) using synthetic aperture radar (SAR) data. Estimation of snow thickness distributions have been attempted using radiometric measurement techniques (Wang et al., 1992), direct backscatter inversion techniques (Beaven et al., 1995) and using the thermal dependence of backscatter (Barber et al., 1998a; 1998b; Yackel

and Barber, 2007). Moreover, fully polarimetric SAR (POLSAR) data has not been extensively evaluated because fully polarimetric sensors (e.g., RADARSAT-2, TerraSAR-X) have only recently become available since 2007. Consequently, the additional information acquired in high resolution fully polarimetric SAR data requires investigation as a complimentary approach for estimation of snow thickness on FYI.

POLSAR data is commonly used in polarimetric decomposition modeling to understand the scattering mechanisms of snow covered sea ice (e.g. van Zyl, 1989; Touzi, 2007; Durden et al., 1989; Ulaby et al., 1990). Most of the polarimetric decomposition models are mathematically constructed (van Zyl, 1989; Freeman and Durden, 1992; 1998; Cloude and Pottier, 1996) and require large numbers of input parameters as compared to output parameters (Freeman and Durden, 1998). Consequently, it is difficult to incorporate the input parameters (namely 'ground truth') from the very sparse number of observation stations to permit the successful discrimination of the ground object (Comiso, 1995).

The "three-component model" proposed by Freeman and Durden (1998) uses radar scattering physics and is based on incoherent decomposition. It is well adapted for natural terrain and agricultural fields (Freeman and Durden, 1992 and 1998). Scheuchl et al., 2002, used this technique to separate sea ice and land on SAR images and to discriminate different ice types on single and dual frequency airborne synthetic aperture radar (AIRSAR) data.

The central aim of this study is to gain an improved understanding of the primary scattering mechanisms over snow covered landfast FYI. A three-component scattering model (Freeman and Durden, 1998) is used to derive the primary scattering mechanisms. Surface scattering is contributed from the boundary between two media (i.e., air-snow or snow-ice) due to the dielectric discontinuities of the medium. If the sea ice surface is rough with respect to the

incident wavelength, much of the signal is scattered back to the source. As such, there is very little or no backscatter observed at a smooth ice (SI) surface. Specular reflection occurs at steeper incidence angles, resulting in low backscatter (Freeman and Durden, 1998; Manninen, 1992). Double-bounce can occur on ice ridges. Volume scattering is mainly contributed from the volume layer between two interfaces. This scattering is stronger at shallower incidence angle compared to steeper incidence angle resulting higher backscatter (Manninen, 1992).

1.2 Objectives

The main objective of this study is to gain an improved understanding of the *three-component* scattering mechanisms over snow-covered landfast first year sea ice. A technique will be investigated that is able to decompose the total scattering coefficient of POLSAR images into a three-component scattering model without incorporating any ground truth data. It also aims to examine how these scattering mechanisms change in the context of various snow-physical properties and polarimetric synthetic aperture radar (POLSAR) incidence angle variations during the spring transition season. In-situ field measurements coincident with spaceborne POLSAR overpass data will allow me to achieve the following specific objectives using two case study sites.

1) to quantify the three primary scattering contributions (i.e. surface, volume and double-bounce) from a heterogeneous snow covered FYI icescape in Hudson Bay, near Churchill, Manitoba,

2) to quantify the sensitivity of proportional contributions of the three-component scattering mechanisms at two different incidence angles (29° and 39°),

3) to quantify the sensitivity of proportional contributions of a three-component scattering mechanism at two different climatic conditions ($-0.4°$ C and $-8.0°$ C) over a group of heterogeneous snow thickness classes on smooth FYI in Franklin Bay, Northwest Territories (NWT).

4) to evaluate the relationship between polarimetric parameters and snow thickness classes at two different surface air temperatures ($-0.4° C$ and $-8.0° C$), and;

5) to identify relatively stable polarimetric parameters and associated radar incidence angles which could be used to estimate snow thickness on FYI.

1.3 Thesis Layout

This thesis contains six chapters and one appendix. A review of fundamentals and nomenclature pertinent to this thesis is provided in Chapter 2.

Chapter 3 introduces the study area, data and field methods conducted during two field seasons. Chapter 4 and 5 contain results and discussions for two case studies: Incidence angle effect of three primary scattering experiments over snow covered FYI and thermal implications of three-component scattering mechanisms of heterogeneous snow cover on smooth FYI. Aspects of several chapters have been submitted for publication in the peer-reviewed literature:

Hossain, M.M., Yackel, J.J., Dabboor, M. (2012). Application of a three-component scattering model over snow covered first-year sea ice using polarimetric C-band SAR data. *International Journal of Remote Sensing.* Sub #: TRES-PAP-2012-0379.39p.

Hossain, M.M., Yackel, J.J. Geldsetzer, T. (*In-preparation*). Observations of snow cover on landfast first-year sea ice in late winter using polarimetric C-band SAR data. *IEEE Transactions on Geoscience and Remote Sensing.* Sub #: TGRS-2012-000X, 40p.

Chapter 6 provides a summary of results and concluding remarks. Suggestions for further research are given. Appendix A provides the results summary tables of polarimetric parameters presented in this thesis.

Aspects of this research have contributed to the following peer reviewed research publications:

Dabboor, M., Yackel, J.J., **Hossain, M.M.,** Burn, A. (2012). Comparing Matrix Distance Measures for Unsupervised Polarimetric SAR Data Classification of Sea Ice Based on Agglomerative Clustering. *International Journal of Remote Sensing.* Accepted. TRES-PAP-2012-0064. 30P.

Fuller, M.C., Gill, J.P.S., **Hossain, M.M.,** Yackel, J.J. (*In-preparation*).Observations of complexly-layered snow on first-year sea ice using microwave remote sensing. *Journal of Geophysical Research-Ocean.*

Chapter Two

FUNDAMENTALS AND NOMENCLATURE

2.0 Introduction

This chapter presents a review of the sea ice development, seasonal evolution of the microwave backscatter coefficient, sea ice geophysical processes, snow properties and polarimetric SAR parameters. These concepts are referenced within the context of snow (dry and/or wet) covered FYI.

2.1 Development of Sea Ice

Arctic sea ice is generally categorized into icebergs and pack ice on the basis of their formation. Icebergs are chunks of floating ice that have broken off from a glacier and they are originally formed from compacted snow. The pack ice is formed by the freezing of seawater and considered as sea ice.

Specifically, the sea ice is the combination of liquid brine, ice and solid salts in a coherent conduct. Sea ice is simply frozen sea water formed when sea surface temperature reaches approximately -1.86^0 C at 34 PSU. As air temperature starts to decline past 0° C, different stages of sea ice are developed. Initially, at 0° C fine spicules or plates of ice begin to originate on the sea surface, which is known as *frazil ice*. This *frazil ice* freezes more and coagulates to form a smooth, thin sheet of ice, called *grease ice*. *Grease ice* has little light reflective capability which gives the sea water a matte appearance. Another stage of sea ice, when snow is saturated and mixed with sea water after a heavy snowfall, is *slush*. Furthermore, the wind and sea waves push up and consolidate slush to another form of ice which is identified as *shuga.* These four stages of sea ice (*frazil ice, grease ice, slush and shuga*) are classified as

New Ice. These types of ice are weakly frozen together and thickness is not more than 10 cm (WMO, 2007).

As thin ice continues to cool and is easily merged under the effect of waves, swells and under ocean pressure, and is declared *Nilas ice. Nilas* can be divided into two sub-categories depending on color and thickness. *Dark Nilas* is very dark in color (< 5 cm thick) and *Light Nilas* (5 to 10 cm) is lighter than Dark Nilas. *Ice Rind* is shaped on a quiet sea surface through freezing of low salinity water and the thickness is ≤ 5 cm. All of three ice types (*Ice Rind, Dark Nilas and Light Nilas)* are considered *Nilas ice.* Another ice type known as *Pancake ice* is formed on the rough ocean and under higher salinity conditions. *Nilas, Ice Rind* and *Pancakes* are known as *Young Ice* which can be further sub-categorised into *grey ice* (10-15 cm thick) and *grey-white ice* (15-30 cm thick) (Maykut, 1978; WMO, 2007).

Young Ice, which lasts for not more than one winter, is known as *First Year Ice (*FYI*)*. The thickness of FYI varies from 30 cm to 2m which is sub-categorized into three separate FYI types on the basis of thickness; *Thin First Year Ice (30-70cm), Medium First Year Ice (70-120cm) and Thick First Year Ice (120cm-2m)* (WMO, 2007).

Thick FYI, which persists beyond only one summer melt, is called *Second Year Ice (SYI)* and if it has survived at least two summers melt it is known as *Multi-Year Ice* (MYI).This *SYI* and *MYI* belong to the group of *Old Ice* with thickness ranging from 120 cm to ~ 5 m (MSC, 2005; WMO, 2007; Weeks and Ackley, 1982). Additional details about sea ice development stages are available in Tucker et al.,(1992).

The topmost FYI is often characterised by its surface roughness or state of deformation. *Smooth FYI* originates from thermodynamic freezing under low wind conditions. *Rough FYI* grows in the combination of wave action with moderately windy weather and its surface

roughness ranges from centimeter to several decimeters in scale (Wadhams, 2000). Another form of FYI is *Deformed ice, which* develops in the presence of thicker FYI, MYI or land with compressive forces; or ridging and rafting happens within FYI (Dierking and Dall, 2007).

2.2 Seasonal Evolution of Arctic Sea Ice

The development of sea ice is important to understand its characteristics and how it grows seasonally (Figure 2.1). The atmospheric conditions, particularly ambient air temperature, play a significant role in sea ice formation. Livingstone et al.,(1987) categorized sea ice development stages, namely *Freeze-up, Winter, Early melt, Melt onset* and *Advanced melt.* These are useful to better understand the thermodynamic evolution of the OSA.

In the Arctic, *freeze-up* stage starts from October-November when the solar radiation and ambient air temperature decrease; thin FYI grows on open water. In December, when solar radiation is negligible and air temperature continues to decline, the thin FYI turns into medium FYI and snow accumulates on its surface. The *winter* stage starts from January and lasts until April; the sea ice properties have comparatively little change due to almost no solar input during January to March. In late April or May, the *early melt* stage begins, when surface air temperature increases with increasing solar input. The *melt onset* stage starts from May or June, when solar input continues to increase and thereby snow surface temperature increases and the snow accumulates some liquid water. The final stage is the *advanced melt,* when most of the snow cover melts and melt ponds appear on the sea ice surface (Barber et al., 2001; Livingstone and Drinkwater, 1991; Sturm et al., 2002; Yackel et al., 2007).

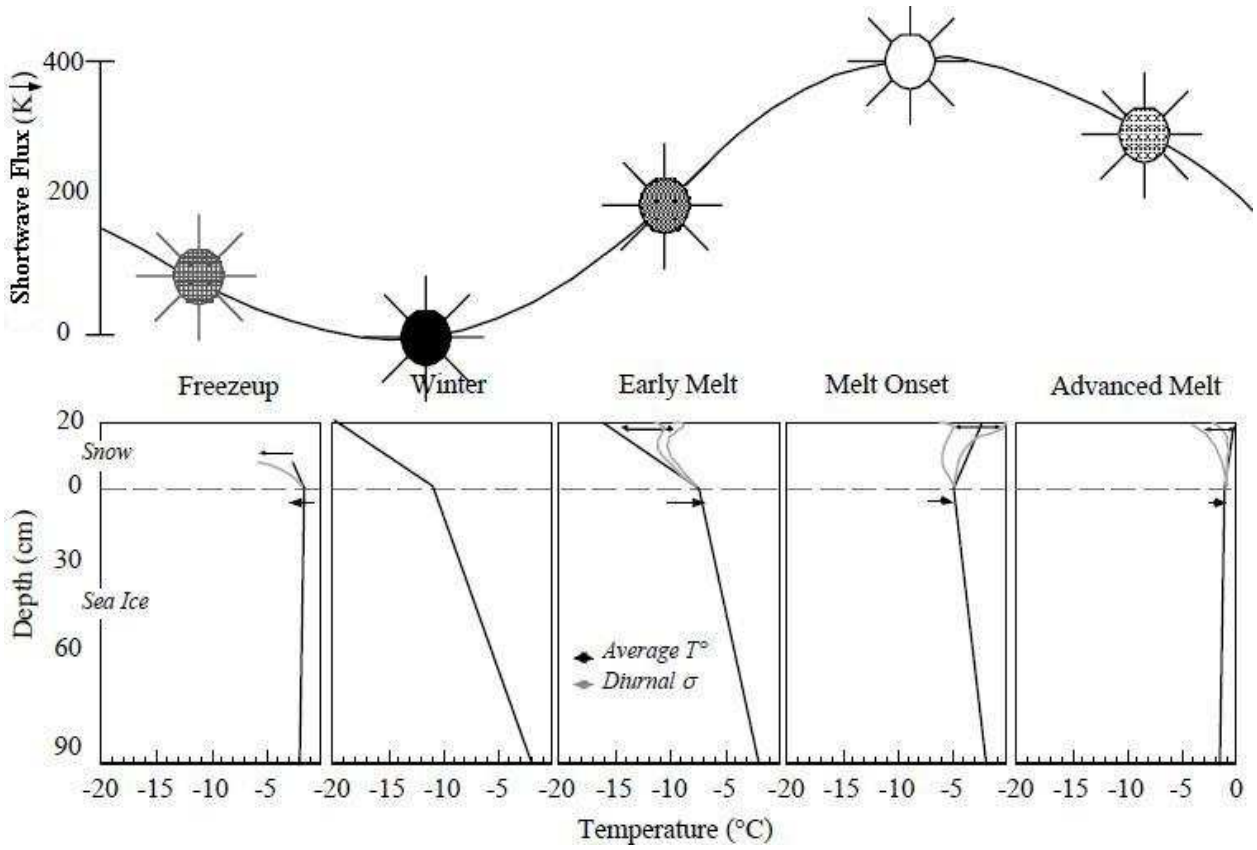

Figure 2.1: Categorical structures discriminating seasonal thermodynamic regimes from freeze-up to advanced melt for landfast first-year sea ice in the Canadian Arctic. Temperature profiles represent nine years of in-situ data. The available shortwave energy is denoted in summary above the thermodynamic profiles (Adapted from Barber et al., 2001).

2.3 Surface Features of Sea Ice

Surface features on sea ice characterize an important component of the OSA system. The thermodynamic and geophysical properties of sea ice are completely dependent on their different surface topography and OSA interactions.

2.3.1 Brine layer within sea ice

Newly formed sea ice mostly contains a thin brine skim. This thin layer can freeze and form a very high salinity skim on the sea ice surface (Ono and Kasai, 1985). It can additionally act as a source of brine for frost flowers (detailed later in this section). The brine layer within the sea ice can be transported towards the surface, but the exact nature of the transport has not been fully verified yet. One idea is that the saline layer is formed by brine expulsion, which is an important process with initial ice formation, but decreases in importance with increasing sea ice thickness (Wettlaufer and Worster, 1995). It can be enhanced since the upper layer of the ice has higher porosity than the underlying ice, providing favorable conditions for the upward transport of brine (Wettlaufer and Worster, 1995). Another theory is that brine can be transported within the ice grain boundaries towards the sea ice surface, as determined by a thermo-molecular pressure gradient (Barber and LeDrew, 1995) as a result of the temperature difference between the warmer underlying ocean and the colder atmosphere.

2.3.2 Snow on sea ice

Snow cover on sea ice has significant ramifications in terms of the thermodynamics, dielectrics, and microwave scattering signatures of the sea ice. Snow on sea ice can be described as a mixture of ice crystals, air, and potential liquid water and/or brine. In illustrating snow cover characteristics the parameters of interest include the thickness, density, temperature, salinity, liquid water content, grain size, and grain structure. Changes to these parameters are based on the formation of the initial snow cover and the thermodynamic evolution of the snowpack as a function of changing air temperature. Snow on sea ice can be separated into layers based upon the physical parameters. Statistics on the grain size, density, and salinity are well established, for example Barber and LeDrew, 1995.

Snow is formed in the atmosphere under a variety of different formation mechanisms and is deposited on the sea ice surface. The density of snow ranges from ~50 to 500 kg/m^3 and gradually increases with age (Sturm et al., 2002). During the winter season, the snowpack is commonly distinguished by three distinctive layers: the new snow layer (grain size 1-2 mm^2), the original snow layer (2-4 mm^2), and the basal snow layer (9-20 mm^2) (Barber and LeDrew, 1995; Colbeck, 1982).

A series of thermodynamic metamorphisms have taken place once snow has fallen on the sea ice surface. The growth processes and temperature gradient in the snow cover determine the size and shape of the snow crystals. Temperature gradient metamorphism plays the most significant role on grain size. The grain growth occurs when wetness is present and the temperature gradient is high enough to expel the brine into the ocean or push it up to the surface (Colbeck, 1983). In the absence of a high temperature gradient the snow grains grow slowly and equally in all directions, creating well rounded crystals which are known as the equilibrium form of snow (Martin et al., 1996).

The temperature of the snowpack is warmer at the bottom compared to the top which can be due to the thermal blanketing effect, resulting in upward vapor transport. Kinetic growth takes place at the basal layer at the bottom of the snowpack where the larger grains grow at the expense of the smaller grains. Moreover, the basal layer of the snowpack is saline due to brine wicking from the sea ice surface and potentially from an old layer of frost flowers which can be contributed into the overlying snow accumulation. The snow grains near the surface of the snowpack are usually more rounded and are not very likely to form kinetic growth forms due to colder temperatures. A typical profile of the snowpack shows that grain size become larger when

it is moving from the air-snow interface layer to the snow-ice interface layer and the density of the snow becomes lower.

2.3.3 Temperature and salinity

Temperature and salinity are two distinct significant characterization parameters of sea ice. In a steady state, temperature is linearly distributed within a sea ice layer from the top interface with cold air to the bottom interface with warmer seawater. Numerous studies of sea ice temperatures show an approximately linear profile in ice thickness (e.g., Cox and Weeks, 1974;Wen et al., 1989; Eicken, 1992). C-shaped salinity distribution is usually observed within FYI (Eicken, 1992). Upward brine expulsion and flooding are important mechanisms, resulting in the high top salinity (Eicken, 1992). The high bottom salinity is obvious due to the interface between ice and relatively saline seawater.

Electromagnetic properties of sea ice are strongly related to the temperature and salinity. These two parameters combine with sea ice density to organize the thermodynamic phase distribution of sea ice constituents. Fractional volumes of brine and air inclusions are measured from equations based on phase diagrams (Cox and Weeks, 1983). Top of the ice surface temperature is relatively low and the salinity is high (C-shaped salinity profile). Deeper into the middle of the ice layer the temperature increases and the salinity decreases. Exceptional results may be observed at the sea-water interface, where the brine volume is relatively large, and the distribution of temperature and salinity is approximately uniform (Wen et al., 1989).

Moreover, temperature governs permittivities of individual constituents of sea ice. Ice permittivity varies with temperature (Tiuri et al., 1984). Brine permittivity is another strong function of temperature (Stogryn and Desargant, 1985), and seawater permittivity depends on

both temperature and salinity (Klein and Swift, 1977). Temperature also influences sea ice effective permittivity by the process of salt expulsion.

2.3.4 Frost flowers

Frost flowers are important features, which develop rapidly on new sea ice under calm conditions. They are recognized by their high salinity (2-3 times oceanic values) and by their crystal growth habits such as clumps, dendrites growing on rods, hexagonal plates, or needles. The frost flowers wick up brine rejected by the sea ice through surface tension. The surface brine comes from the interior based upon mass balance relations (Martin et al., 1995). Several observations have shown that the flowers insulate the ice surface from the colder air by several degrees. However, radar measurements are sensitive to the presence of the frost flowers, demonstrating a substantial increase in backscatter when the flowers are present.

2.4 Active Microwave Remote Sensing of Sea Ice

The aim of active microwave remote sensing of sea ice is to gain information on the geophysical or thermo-physical state of the sea ice through backscattering measurements. The physical composition of the sea ice fabric and snow cover can be switched into an electrical description through the dielectric concept. The propagation of electromagnetic waves in the sea ice medium is dependent upon the radar system parameters and the sea ice dielectrics.

2.4.1 Microwave backscatter from snow covered FYI

Microwave backscatter from a porous media such as snow covered FYI is a function of surface, volume and double-bounce scattering, which is largely determined by a combination of geophysical properties of snow and sea ice (Fung, 1994). The backscatter response is best understood as the sum of the contributions by interaction mechanisms illustrated in Figure 2.2.

Backscatter response also depends on microwave penetration depth, which is a function of microwave frequency, incidence angle, and dielectric properties of the media including snow density and wetness. The penetration depth of C-band microwaves into cold (i.e. $< -8°$ C) snow over FYI is on the order of 30 to 60 cm, with penetration into FYI, of frazil structure, on the order of a few cm to a maximum of 5 cm (Drinkwater et al., 1991; 1992).

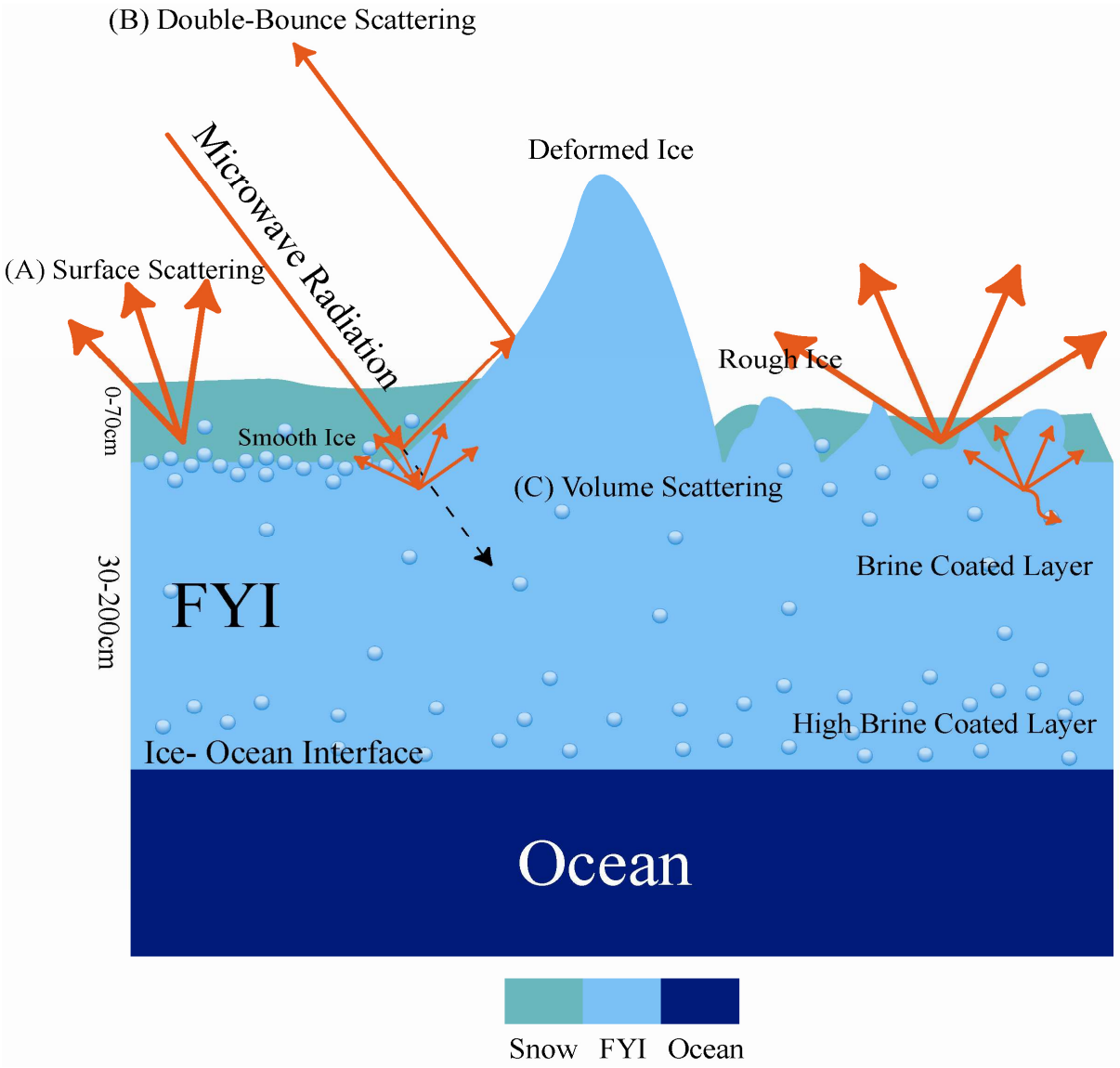

Figure 2.2: Conceptual schematic illustrating a three-component scattering mechanism over snow covered FYI demonstrating: (A) surface, (B) double-bounce and (C) volume scattering mechanisms (Adapted from Fung, 1994). "Bubbles" within the snow and the FYI layers indicate either enlarged brine coated snow grains, hoar crystals, air bubble inclusions, or brine inclusions; all of which contribute to volume scattering (Barber and Nghiem, 1999).

2.5 Polarimetric SAR Parameters

2.5.1 Three-component scattering model

Freeman-Durden polarimetric decomposition theorems segregate the reflected scattering signal into the three scattering contributions which can be used for discriminating targets (e.g. snow covered FYI) in POLSAR imagery. Consequently, different decomposition techniques have been used to analyze and interpret POLSAR images (Cloude and Pottier, 1996) and are based on the complex scattering matrix or the coherency/covariance matrix. This decomposition relies on the conversion of covariance matrix $[C]$ to the three-component scattering model (Freeman and Durden, 1998). Thus, the decomposition model decomposes the total scattering power into three scattering processes: surface (P_s), double-bounce (P_d) and volume (P_v) scattering.

The microwave scattering matrix [M] can be expressed by following the reciprocity theorem of Ulaby and Elachi, 1990, in equation 1:

$$[\mathrm{M}]=\begin{bmatrix} M_{yy} & M_{yx} \\ M_{xy} & M_{xx} \end{bmatrix} \tag{1}$$

where the first index represents the received polarization and the second represents the transmitted polarization. We can express $[M]$ as a covariance matrix $[C]$ to explain complex backscatter information in equation 2:

$$[\mathrm{C}]=\begin{bmatrix} \langle M_{xx}M_{xx}^{*}\rangle & \langle M_{xx}M_{xy}^{*}\rangle & \langle M_{xx}M_{yx}^{*}\rangle & \langle M_{xx}M_{yy}^{*}\rangle \\ \langle M_{xy}M_{xx}^{*}\rangle & \langle M_{xy}M_{xy}^{*}\rangle & \langle M_{xy}M_{yx}^{*}\rangle & \langle M_{xy}M_{yy}^{*}\rangle \\ \langle M_{yx}M_{xx}^{*}\rangle & \langle M_{yx}M_{xy}^{*}\rangle & \langle M_{yx}M_{yx}^{*}\rangle & \langle M_{yx}M_{yy}^{*}\rangle \\ \langle M_{yy}M_{xx}^{*}\rangle & \langle M_{yy}M_{xy}^{*}\rangle & \langle M_{yy}M_{yx}^{*}\rangle & \langle M_{yy}M_{yy}^{*}\rangle \end{bmatrix} \tag{2}$$

These four-by-four Hermitian matrices characterize fully POLSAR backscattering properties of sea ice (Zebker and van Zyl, 1991; Drinkwater and Kwok, 1991).

Surface scattering from the snow-air and snow-sea ice interfaces is influenced by snow grain size, density discontinuity, degree of roughness and electrical discontinuities of the material and the interface radar incidence angle (Fung, 1994). The double-bounce scattering mechanism is modeled by combinations of backscatter from the snow-ice surface and ice ridges, which act as a dihedral corner reflector. The horizontal snow-covered ice surface (ss) has Fresnel reflection coefficients M_{ssx} and M_{ssy} for horizontal and vertical polarizations, respectively. Thus, the vertical ice ridge (ir) has reflection coefficients M_{irx} andM_{iry}. The model can be made more accurate by integrating propagation factors $e^{2j\gamma x}$ and $e^{2j\gamma y}$, where γx and γy are the complex coefficients. Volume scattering usually occurs from the snow basal layer where enlarged brine coated grains, and brine inclusions are largely found (Barber et al., 1995) (Figure 2.2). The mathematical expression of the three-component scattering model is given in equation 3 by using a 4×4 covariance matrix $[C_4]$ after Freeman and Durden 1992; 1998:

$$[C_4] = P_s\,[C_4]_s + P_d[C_4]_s + P_v\,[C_4]_s \qquad (3)$$

2.5.2 Polarimetric radar parameters

The polarimetric radar parameters employed in this study are computed from equations 1 and 2, namely, the microwave scattering matrix M and covariance matrix C, respectively. The detailed descriptions of those parameters: co- and cross-pol ratios and span described in equation 4-6 are discussed in Drinkwater et al., (1992).

2.5.2.1 *Co- and cross-polarization ratios*

The statistical proportion between$\sigma_{xx}^0\sigma_{xx}^0$, $\sigma_{yy}^0\sigma_{yy}^0$ and $\sigma_{xy}^0\sigma_{xy}^0$ are denoted as the co-polarization ratio (co-pol,$\gamma_{co}\gamma_{co}$) and the cross-polarization ratio (cross-pol,$\gamma_{cr}\gamma_{cr}$). The c*o- and cross-polarization ratios* describe the scattering mechanism, orientation of the scatterer and characteristics of the surface roughness (Drinkwater et al., 1992). Here |■| denotes the modulus of a complex number.

$$\gamma_{co} = \frac{\sigma_{xx}^0}{\sigma_{yy}^0} = \frac{|M_{xx}|^2}{|M_{yy}|^2} \quad (4)$$

$$\gamma_{cr} = \frac{\sigma_{xx}^0}{\sigma_{xy}^0} = \frac{|M_{xx}|^2}{|M_{xy}|^2} \quad (5)$$

2.5.2.2 *Total Power (SPAN)*

The total power (T_p) or *SPAN* of POLSAR is the combined intensities of the diagonal elements or trace of the scattering matrices. It contains the multidimensional information provided by the scattering matrix in a single image (Cloude and Pottier, 1997). The mathematical expression of SPAN is presented in equation 6.

$$T_p = SPAN = \sigma_{xx}^0 + 2\sigma_{xy}^0 + \sigma_{yy}^0 = |M_{xx}|^2 + |M_{xy}|^2 + |M_{yx}|^2 + |M_{yy}|^2 \quad (6)$$

2.5.2.3 *Co-polarization Phase Difference*

The φ_{xx-yy} φ_{xx-yy}(Equation 7) is a measure of the two co-polarized channels, (xx, yy) average phase angle differences from $-180°$ to $+180°$ and directly corresponds to the number of bounces an incident wave experiences during reflection (Evans et al., 1988). The $\varphi_{xx-yy}\varphi_{xx-yy}$

trends to increase with incidence angle for a plane dielectric surface at a rate determined by the dielectric permitivity and is useful for separating ice types based on age, as well as open water, new ice, and old ice (Drinkwater et al., 1992). The previous studies showed the value close to zero for cold MYI hummock ice (sea ice piled haphazardly one piece over another to form an uneven surface); intermediate for cold, saline FYI; and high for a shallow, wind-roughened melt ponds on FYI (Geldsetzer et al., 2007). Here ⟨■⟩ denotes the average over number of pixels. *Im and Re* represent imaginary and real number respectively.

$$\varphi_{xx-yy} = tan^{-1}\left[\frac{Im\langle M_{xx}M_{yy}^{*}\rangle}{Re\langle M_{xx}M_{yy}^{*}\rangle}\right] \varphi_{xx-yy} \quad (7)$$

2.5.2.4 *Co-polarization correlation coefficients*

The co-polarized correlation coefficient (μ_{xxyy}) (μ_{xxyy})decreases with increasing incidence angle over sea ice that is predominantly surface scattering (e.g. FYI under cold weather conditions) at a rate determined by salinity. Nghiem et al (1995) attribute lower values of μ_{xxyy} to anisotropy in the shape and orientation of sea ice dielectric inclusions in volume scattering situations. The magnitude of μ_{xxyy} also decreases when there is an anisotropic mix of scattering mechanisms within the resolution cell for a distributed target (Thomsen et al., 1998). Geldsetzer et al (2007) showed a greater rate of decrease for FYI compared to MYI under cold climatic conditions using surface-based polarimetric C-band SAR data.

$$\mu_{xxyy} = \left[\frac{\langle M_{xx}M_{yy}^{*}\rangle}{\sqrt{\langle M_{xx}M_{xx}^{*}\rangle\langle M_{yy}M_{yy}^{*}\rangle}}\right] \quad (8)$$

2.5.2.5 *Fractional polarization*

The fractional polarization (F_p) is defined by equation 9. The degree of polarization of a reflected wave can be written in the form of $\left(\frac{P_{max}-P_{min}}{P_{max}+P_{min}}\right)$, where P_{max} and P_{min} are the received intensity extrema when only the received polarization varies. Touzi et al (1992) used the F_p as a measure of the polarization intensity of the return.

$$F_p = \frac{P_{max}-P_{min}}{P_{max}+P_{min}} \quad (9)$$

2.5.3 Target decomposition parameters

The target decomposition parameters, Entropy(H), Anisotropy (A) and Alpha angle (α) in equations 10-12, respectively, are used in this study and are described in detail in Cloude and Pottier (1997). These parameters are able to decipher the proportional contribution of the dominant scattering mechanisms.

2.5.3.1 *Entropy, Anisotropy and Alpha Angle*

The scattering entropy H is an indicator of randomness in scattering mechanisms, and is normalized from 0 to 1. It is computed from the eigenvalue of the covariance or coherence matrix of the target scattering matrix defined in Cloude and Pottier (1997). Each eigenvalue is correlated to the ratio of total scattering power which is contributed from surface, volume and double-bounce scattering mechanisms. The scattering entropy can be expressed mathematically in equation 10. The polarimetric anisotropy (A) defines the relation between the second and the

third eigenvalues, and is a measure for the difference of the secondary scattering mechanisms. where $\delta_2\delta_2$ and $\delta_3\delta_3$ are the eigenvalues of the coherency matrix presented in Cloude and Pottier (1997). The mathematical expression of polarimetric A is presented in equation 11.

$$H = \sum_{i=1}^{3} V_i log_3 V_i \quad (10)$$

$$A = \frac{\delta_{1-}\delta_2}{\delta_1+\delta_2} \quad (11)$$

where V_i indicates i-th normalized eigenvalue and δ_1 and δ_2 are the eigenvalue of coherency matrix [T] which is described in equation 12.

$$[T] = [U_3]\begin{bmatrix}\delta_1 & 0 & 0\\ 0 & \delta_2 & 0\\ 0 & 0 & \delta_3\end{bmatrix}[U_3]^* \quad (12)$$

where [] is the diagonal eigenvalue matrix of [T] and δ_1, δ_2 and δ_3 are eigenvalues of [T] and $[U_3]$.

Alpha angle (α) highlights the nature of the dominant scattering mechanism of the target and is calculated from the eigenvectors of the coherency matrix presented in Cloude and Pottier (1997). The alpha angle is calculated directly from the elements of the eigenvectors as in equation 13:

$$\alpha = P_1\theta_1 + P_2\theta_2 + P_3\theta_3 \quad (13)$$

The value of the alpha angle is ranges from 0° to 90°. The alpha angle $\alpha = 0°$, represents a smooth surface or trihedral isotropic scattering where $|xx| = |yy||xx||yy|$. The value of $\alpha = 45°$ indicates dipole scattering and the surface becomes anisotropic where$|xx| \neq |yy||xx| \neq |yy|$. The maximum value $\alpha = 90°$ defines dihedral or even-bounce scattering.

2.6 Summary

Chapter two has presented a basic overview of sea ice development, seasonal evolution round the year and surface features, with an emphasis on brine layer, snow, temperature, and salinity. Active microwave remote sensing employed in snow covered sea ice research, microwave C-band SAR propagation through snow covered FYI, fully polarimetric C-band SAR parameters have been discussed. An understanding of these concepts is necessary to the methods and analysis in this study. Chapter three presents the study area, field methods employed to acquire meteorological data, in-situ geophysical data, and fully polarimetric C-band SAR data analysis techniques.

Chapter Three

DATA AND METHODS

3.0 Introduction

This chapter discusses the study area, data, data collection and analysis techniques used in this thesis. The study area section describes the geographical setting and a description of the icescape. The data section describes the meteorological data, satellite data and in-situ snow measurement data for both case studies. It also contains field data collection and analysis techniques for both cases which is presented in a separate section.

3.1 Study Area

a. Hudson Bay, MB

The study area is located on landfast FYI in the southwestern coast of Hudson Bay, Canada (Figure 3.1). Hudson Bay becomes completely covered by sea ice during winter (Dec-Jan), and becomes ice-free from mid-August to late October each year (Wang et al., 1994a; Gough et al., 2004). The seasonal sea ice grows to a range of 0.4-2.0 m thick and ice break-up usually starts in early July (Gough et al., 2004; Tivy et al., 2011). The study area is comprised of various forms of landfast FYI (i.e. smooth, rough and deformed ice) as shown in Figure 3.2. The fieldwork for this study was conducted from April 4 to May 29, 2009 to measure in-situ meteorological conditions, snow and sea ice properties.

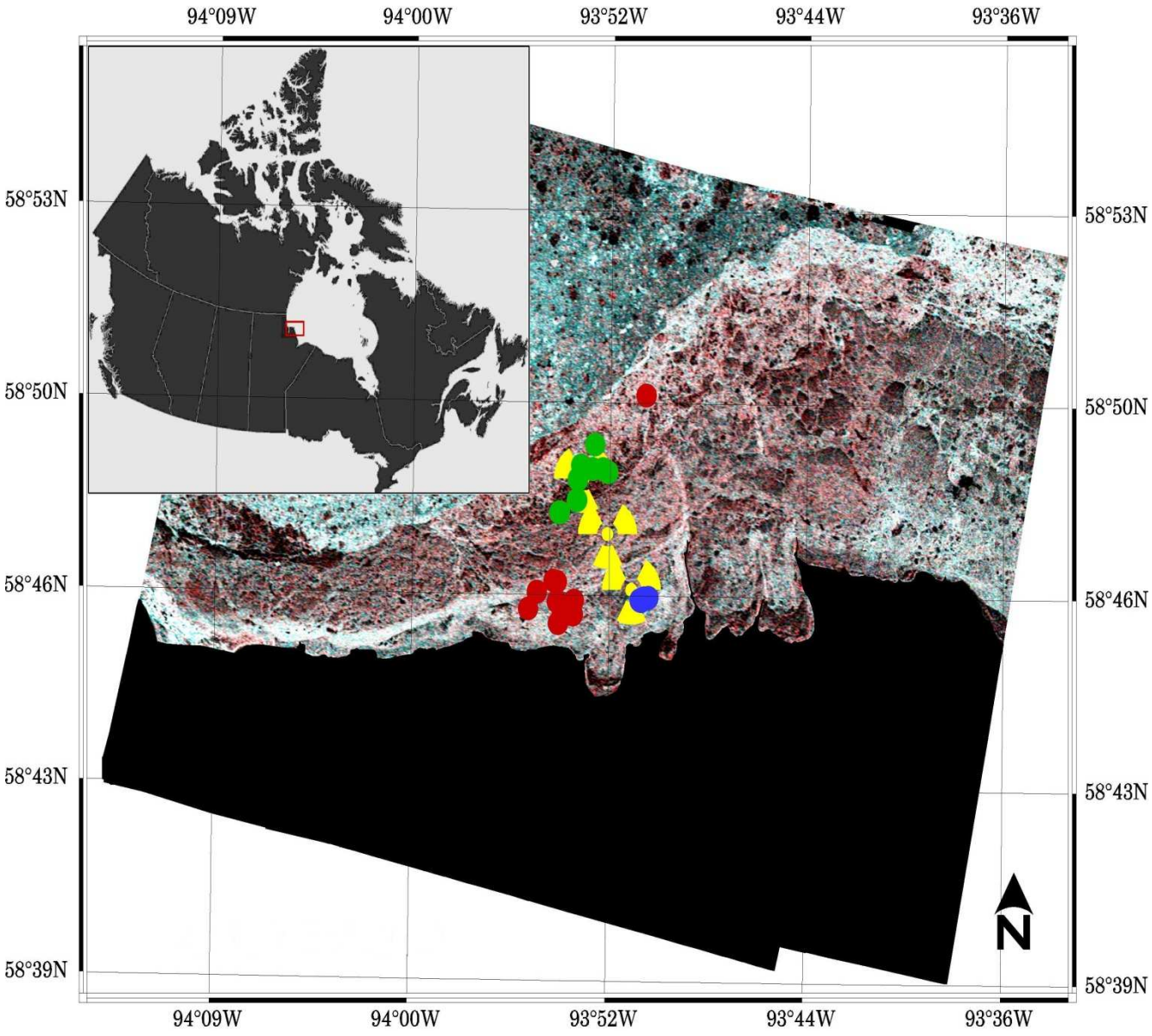

Figure 3.1: Map of Canada (top), overlaid by red box showing the study area in the south-western Hudson Bay, MB, Canada. False color composite (R: σ^0_{xx}, G: σ^0_{xy}, B: σ^0_{yx}) subset of fully polarimetric RADARSAT-2 (C-band) SAR image acquired on May 15 and 18, 2009 at 39° and 29° in descending mode. The green, blue and red color circle represents smooth, rough and deformed ice in-situ sites, respectively. The yellow flag represents the location of three meteorological stations in the field.

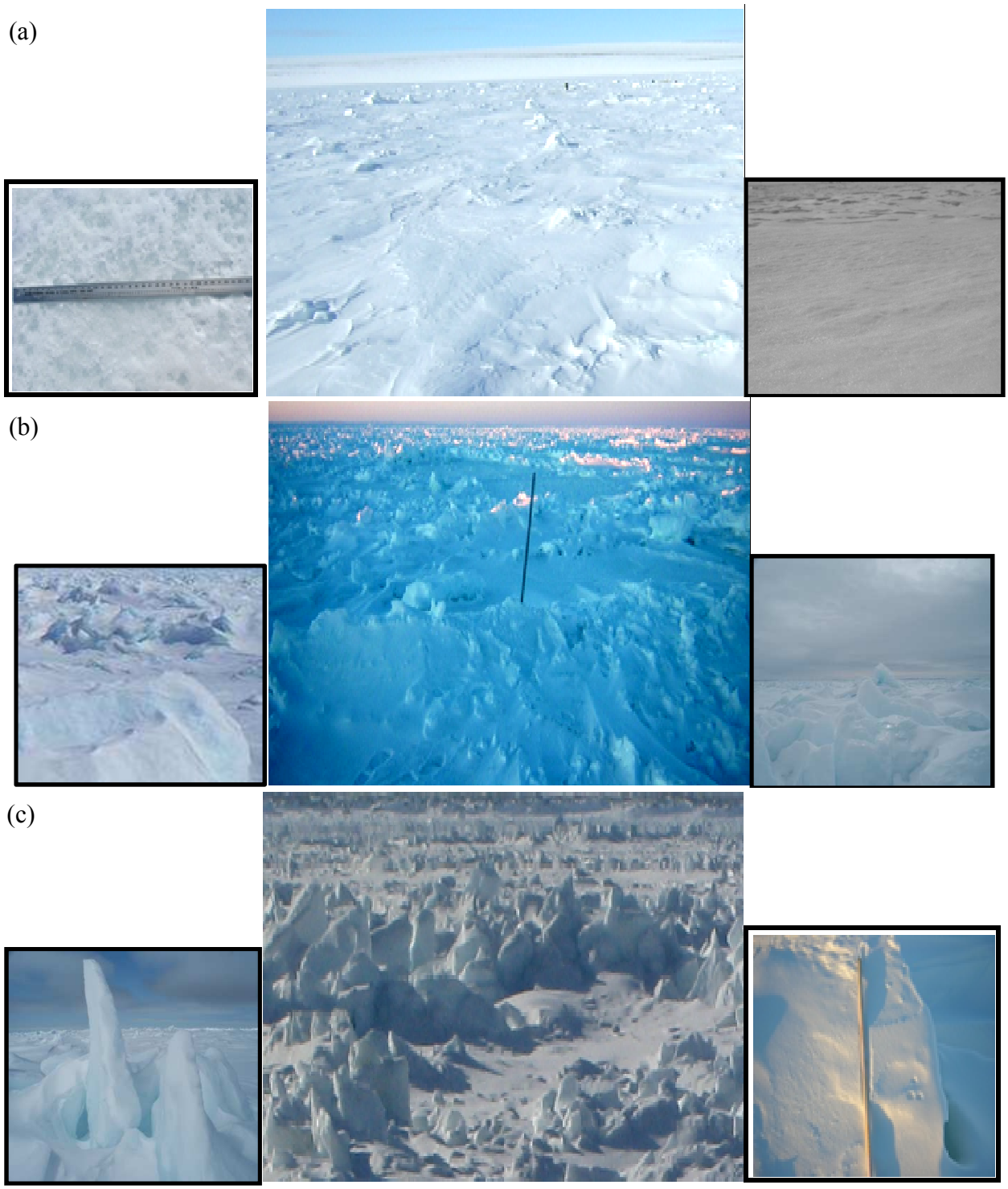

Figure 3.2: Two meter high oblique photographs of various snow covered sea ice surface types within the study area. a) smooth ice (SI), b) rough ice (RI), and c) deformed ice (DI). 1-m rulers are located within some photos for scale. Smaller scale photos with rulers (left and right) reflect snow surface roughness whereas smaller scale photos (middle) reflect the ice surface roughness.

b. Franklin Bay, NWT

The study area consists of landfast first year sea ice (FYI) and marginal ice located on the west coast of Parry Peninsula in Franklin Bay (70° N-125° W), Northwest Territories (NWT),Canada shown in Figure 3.3. This study was part of the International Polar Year-Circumpolar Flaw Lead (IPY-CFL) campaign from April to June, 2008. Franklin Bay measures 48 km long and 40 km wide at its mouth.

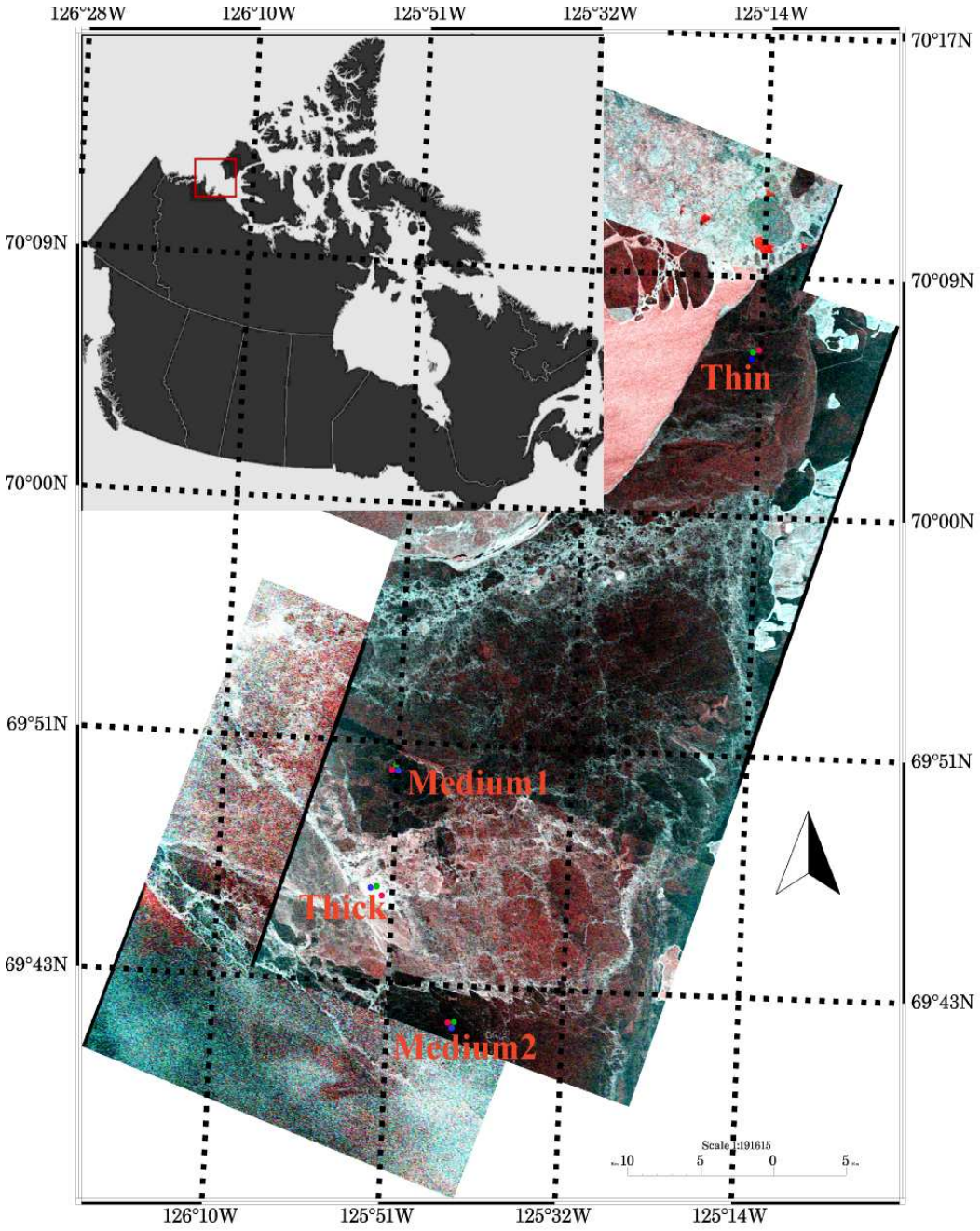

Figure 3.3: Map of Canada (top-left), overlaid by red box showing the study area (Amundsen Gulf) in the western Canadian Archipelago. False color composite mosaic (R: σ^0_{xx}, G: σ^0_{xy}, and B: σ^0_{yx}) of four fully polarimetric RADARSAT-2 SAR images acquired on May 4th and May 14th, 2008 within Franklin Bay, west coast of Parry Peninsula, NWT, Canada. All of the SAR images were acquired in descending mode with separate radar incidence angles of 27.8° and 23.2°. Four different snow sampling sites are overlaid on the images namely Thin, Medium1, Medium2, and Thick, which correspond to the general thickness of the snow cover.

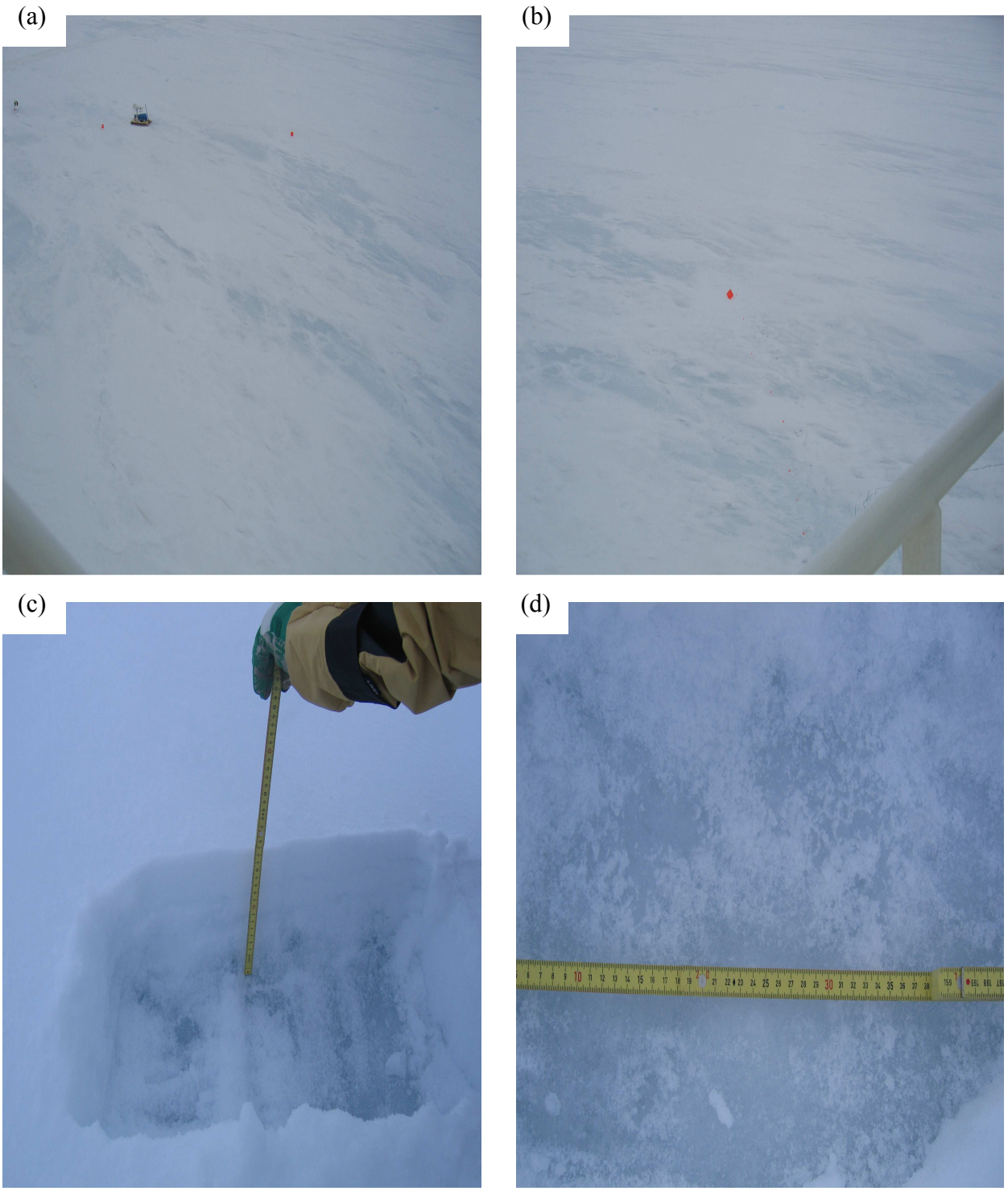

Figure 3.4: Two meter high oblique photographs of various snow covered smooth sea ice surface types within the study area. a) snow transect sites, b) snow covered smooth ice, c) excavated snow pit, and d) ice surface. 1-m rulers are located within some photos for scale of snow surface roughness.

3.2 Data

3.2.1 Meteorological data

a. Hudson Bay

Meteorological data were collected from three stations within the study area located at 58°49.220N, 93°54.219W; 58°47.862N, 93°52.708 W and 58°46.911 N, 93°51.608 W (Figure 3.1). Surface air temperature (SAT) was collected hourly from 1m above the snow surface using a Veriteq Spectrum 2000 ($\pm 0.15° C$) sensor and precipitation amount was measured with Nipher-shielded snow gauge ($\pm$ 0.002 mm) manufactured by Onset Scientific Ltd. The height of the measuring instruments was kept constant at the meteorological stations for all observations during the study period. The daily mean SAT did not exceed $-7.5° C$ during the May 15 to May 18, 2009 period and there was no measureable precipitation.

b. Franklin Bay

Meteorological data consisting of hourly and daily SAT's were acquired from Environment Canada (EC) Cape Parry meteorological station (70.17° N, 124.72° W) and precipitation was obtained from the EC Paulatuk meteorological stations located at 70.10° N, 124.43° W and 69.35° N, 124.08° W (Figure 3.5). The daily mean SAT ranged from $-\ 9.7° C$ to $-0.3° C$ during the field experiment period from May 1st to May 15th, 2008. The surface air temperatures of $-7.9° C$ and $-0.9° C$ were recorded from the Cape Parry station on May 4th and May 14th during the RSAT-2 image acquisition. No significant precipitation events were measured during the study period selected for this experiment (Figure 3.6). Approximately 1 mm of precipitation fell over the region on May 15th, one day following the final SAR image used in this study.

Figure 3.5: Location map of the environment Canada meteorological station of the Cape Parry and Paulatuk in the context of Beaufort Sea and Arctic Ocean.

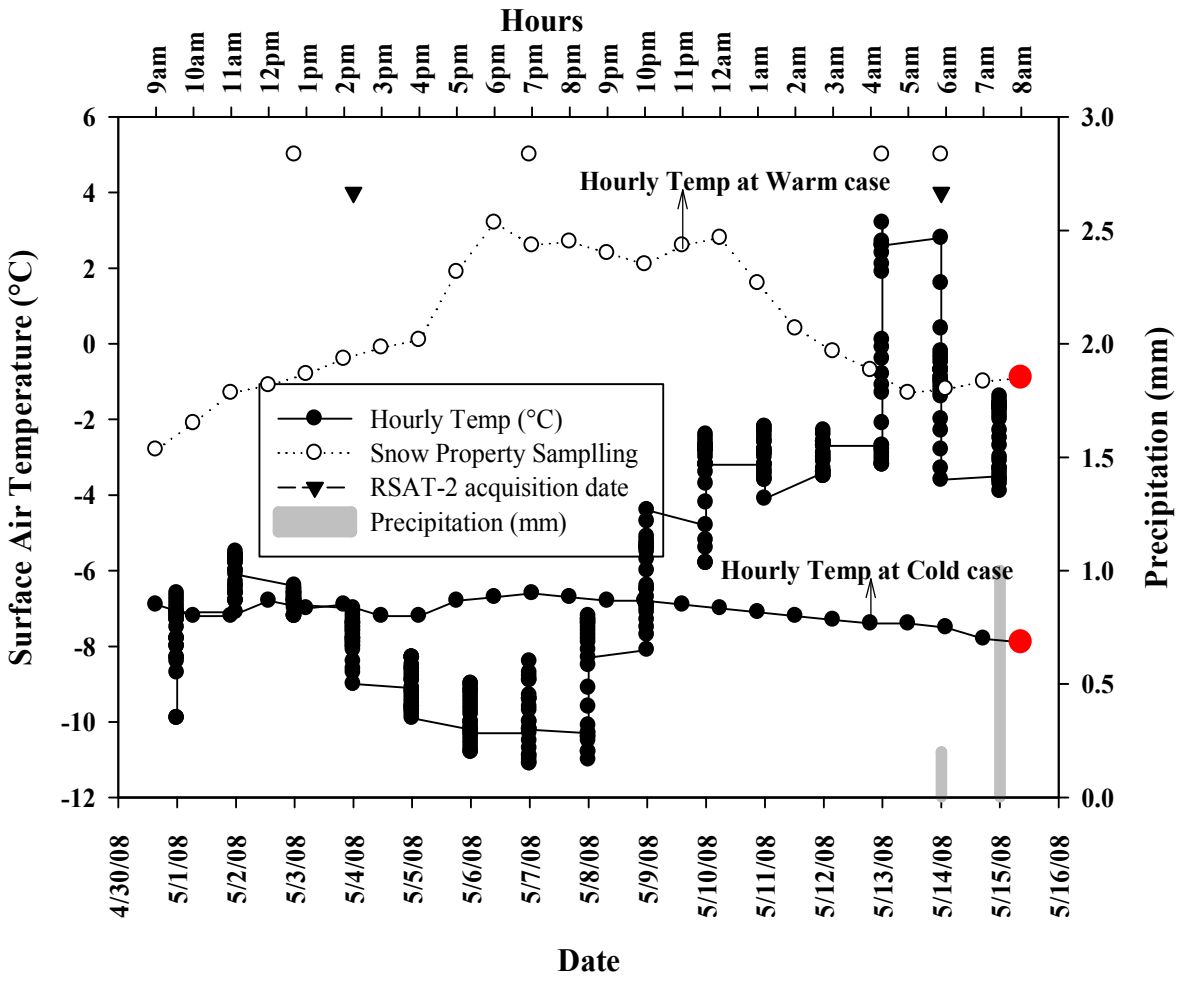

Figure 3.6: Hourly and daily mean surface air temperatures were measured at Cape Parry meteorological station during April 30 to May 16, 2008. Daily precipitation was recorded at Paulatuk meteorological station (Figure 3.5). RADARSAT-2 acquisition times and SAT's are indicated with red dot on hourly temperature plot.

3.2.2 Satellite data

a. Hudson Bay

Polarimetric RADARSAT-2 C-band SAR data was acquired during the period April 4 to May 29 2009 over the study region. All of the selected images consist of Fine Quad-Pol (HH VV HV VH) data with spatial resolutions ranging between 5.2 and 7.6 meters and scene centers ranging from 29° to 39° incidence angle. Two images (May 15 and 18, 2009) were selected for this analysis. Table 3.1 summarizes the image acquisition time (UTC), beam mode, and corresponding daily mean SAT.

Table 3.1: Details of the RADARSAT-2 data used in the study and daily mean SATs of the dates for Hudson Bay

Date	Time (UTC)	Local Time	Scan Dir.	Beam Mode	Incidence angle (°)	Air Temp (°C)	No. of Images
2009-05-15	12:34:06	7:34:06	Desc	Fine Quad-Pol	38.38-39.85	-8.5	1
2009-05-18	12:46:36	7:46:36	Desc	Fine Quad-Pol	28.06-29.82	-9.6	1

b. Franklin Bay

Polarimetric RADARSAT-2 C-band SAR data used in this study was acquired on May 4th and May 14th, 2008. All of the selected images consist of Fine Quad-Pol (HH VV HV VH) data with spatial resolutions ranging between 5.2 and 7.6 meters and scene centers ranging between 23.2° and 27.8° incidence angle. Table 3.2 lists the image acquisition time (UTC), beam mode, and corresponding daily mean SAT.

Table 3.2: Details of the RADARSAT-2 data used in the study and surface air temperature during the satellite image acquisition for Franklin Bay

Date	Time (UTC)	Local Time	Scan Dir.	Beam Mode	Incidence angle (°)	Air Temp (° C)	No. of Images
2008-05-04	15:18:24	08:18:24	Desc	Fine Quad-Pol	26.9-28.8	−7.9	2
2008-05-14	15:26:42	08:26:42	Desc	Fine Quad-Pol	22.3-24.2	−0.9	2

3.2.3 Geophysical data for Franklin Bay

a. Snow thickness measurements

Snow thickness was measured at four different locations over smooth FYI sites of varying surface roughness during the field experiment period from May 3rd to May 14th, 2008. The four validation sites were sampled for snow depth measurements with each measurement site consisting of two transects, one parallel and one perpendicular to the predominant snowdrift pattern. Between 40 to 104 snow thickness samples were acquired in each direction due to time constraints for helicopter scheduling. Snow thickness measurements were taken from the ice surface at 1 meter intervals to the nearest centimeter using a meter stick. Each site center location was recorded using a global positioning system (GPS) receiver.

b. Temperature distribution at snow-ice interface

Snow-ice interface temperatures were modeled from the daily mean surface air temperature (SAT), snow thickness ranging 8 cm to 36 cm (field measurement, May 4-14th, 2008), and ice thickness maximum > 120 cm (Canadian Ice Service, CIS, May 4-14th, 2008), thermal conductivity (ice: $5 \times \frac{10^{-3}\frac{cal}{cm}}{s}/deg$, Schwerdtfeger,1963; snow: $6 \times \frac{10^{-4} calcm}{s}/deg$, Mellor, 1977), snow density ($\sim 0.35\, g.cm^{-3}\ field\ measurement, 2008$) and melting point of ice ($-1.8°\ C$). Snow-ice interface temperature was computed using a simple 1-D thermodynamic model (Nakawa and Sinha, 1981). The results show significant snow-ice interface temperature

variation for thin snow cover as compared to thick snow cover. This is due to the thermodynamic effects on snow cover FYI (Table 3.3).

Table 3.3: Mean (standard deviation) thickness for the four snow thickness classes. Measured daily mean air (Ta) and modeled snow-ice interface (Ti) temperatures for each snow thickness class, for RADARSAT-2 SAR image acquisition dates of May 4th and May 14 th, 2008.

Snow Class	Snow Thickness (cm)	Ta_May4 th (°C)	Ti_May4th	Ta_May14th	Ti_May14th
Thin	8.0(4.0)	−8.0	−6.8	−0.4	−0.7
Medium 1	17.6(9.1)	−8.0	−5.9	−0.4	−0.9
Medium 2	21.5(7.3)	−8.0	−5.6	−0.4	−0.9
Thick	36.4(19.8)	−8.0	−4.8	−0.4	−1.1

3.3 Data analysis techniques

a. Hudson Bay

The May 15 and 18, 2009, images were selectively acquired in similar surface weather conditions (Table 3.1) but at various incidence angles to compare how proportional contributions of three-component scattering mechanisms change with radar incidence angle. To compute the three-component scattering mechanism utilizing the Freeman-Durden decomposition and POLSAR parameters from RADARSAT-2 images, a multi-step data processing approach is applied. First, C-band SAR image data were calibrated to a backscatter coefficient (sigma naught, σ^0) and pre-processed to compute Freeman-Durden decomposition and POLSAR parameters (Freeman, 1992). The polarimetric boxcar 9x9 speckle filter (Lee et al., 2008; Lee et al., 2002) was used to reduce constructive and destructive interference (noise) and to increase the Equivalent Number of Looks (ENL). ENL is used to measure the noise reduction level on POLSAR images and is used to compute several polarimetric parameters which require an ENL ≥ 25. Then the computed decomposition and POLSAR parameters were extracted simultaneously from the two POLSAR images. The region of interest (ROI) for each FYI type

was digitized by overlaying the ground truth points (GTPs) to extract the common ROIs for each FYI type (Figure 3.1). Figure 3.2 illustrates the typical icescape for each FYI type. The ROIs selected identified three different landfast FYI types (Figure 3.1), namely smooth ice (SI), rough ice (RI), and deformed ice (DI). Each ice class contains 200 pixels and each polygon is rectangular in size ($>= 20$ pixels), which is changeable depending on the morphology of homogeneous sample areas. These sample pixels were used to compute mean scattering values and POLSAR parameters.

b. Franklin Bay

Four polarimetric C-band SAR images were selected for this study to quantify the sensitivity of polarimetric parameters and three component scattering mechanisms at two different daily mean surface air temperatures ('Cold' −8.0° C and 'Warm'−0.4° C). The region of interest (ROI) for each snow thickness class was digitized by overlaying the ground truth points (GTPs) to extract the common ROIs for each snow thickness class. The ROIs selected (three 200 m radius buffer circles) correspond to the four different snow thickness class site locations described in the previous section, namely thin (8 cm), medium 1 (17 cm), medium 2 (21 cm), and thick (36 cm). Each ROI contained 1839 pixels and each class consists of three individual sub-groups where each group contains 613 pixels (Figure 3.7). During sample selection a sub-group area was accepted if it represented a visually homogeneous sample for each snow class. This sample site also followed SAR backscattering coefficient ($< -13.54\, dB$) values to provide sufficient evidence that all of the four sampling sites are located over smooth FYI (Lundhaug, 2002). These sample pixels were used to compute absolute and proportional scattering values, and polarimetric parameters.

The number of samples extracted for each group was sufficient to use a one way analysis of variance (ANOVA) test for this study to evaluate the importance of the various polarimetric parameters in distinguishing snow thickness classes from the POLSAR images (Topouzelis et al., 2008; Barber and LeDrew, 1991). ANOVA was used to test the differences among the three individual sub-groups and between the two independent snow thickness classes. First, a within-class ANOVA was used to test for significant variability within each of the four snow thickness classes. The null hypothesis (H_0) of ANOVA states that there is no significant difference between the POLSAR parametric values of snow class pixels of the four different sites at two climatic regimes. The alternative hypothesis (H_1) states that there is significant difference between the POLSAR parametric values of snow class pixels. The independence of cases, normality and homogeneity of variances were computed before performing the test. It is also acknowledged that some spatial autocorrelation will exist within each of the samples.

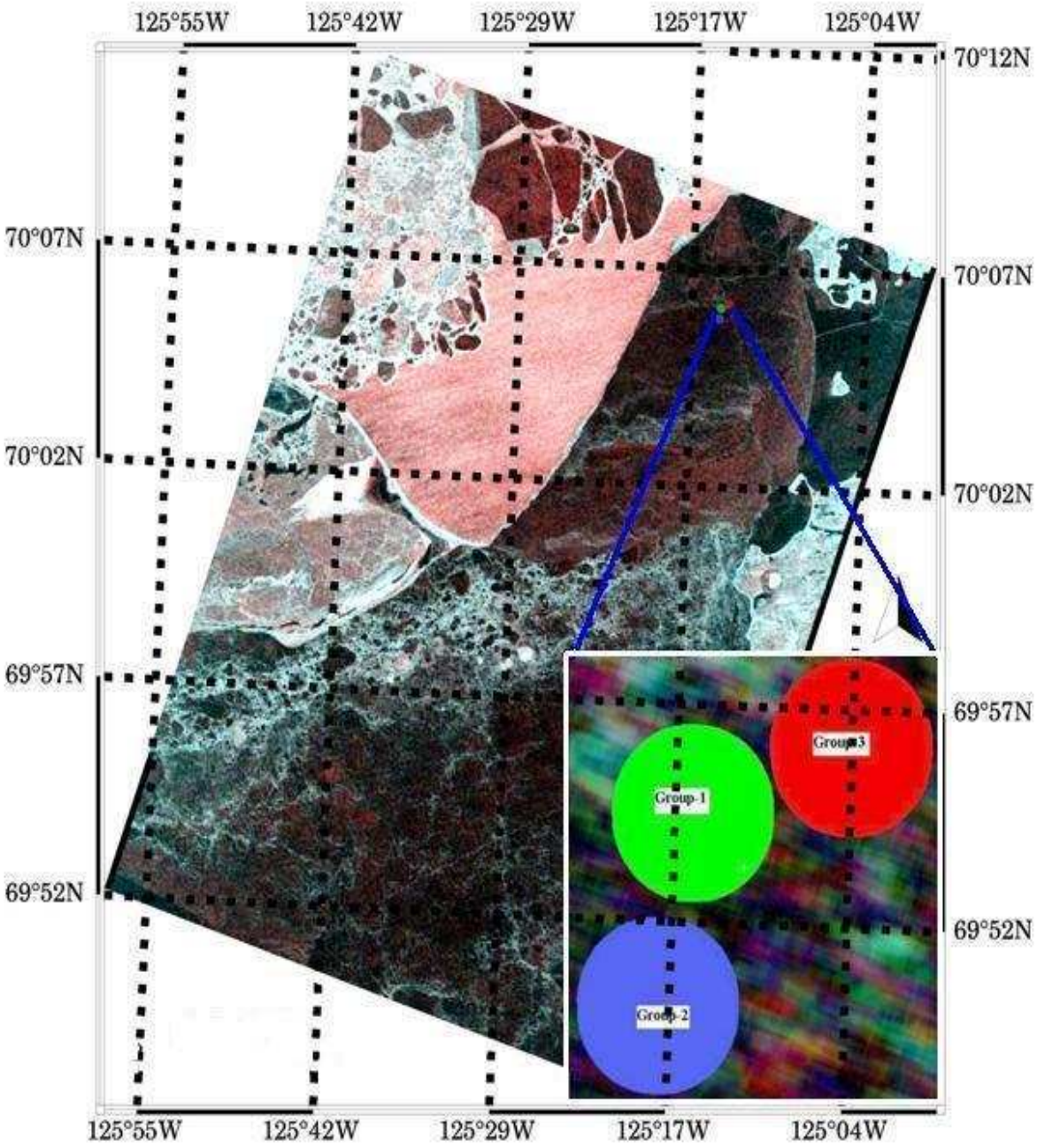

Figure 3.7: False color composite (R: σ^0_{xx}, G: σ^0_{xy}, and B: σ^0_{yx}) subset of RADARSAT-2 SAR image showing the location of selected 'within-site' samples on thin snow covered smooth FYI within the landfast region of Franklin Bay, NWT. Inset map illustrates the method of randomly acquiring three sample groups of pixels to test for 'within-site' variability.

3.4 Summary

Chapter three has presented a description of the two case study areas and sampling site as well as climatic condition and geographic location. It has described the tools used in the meteorological, and snow covered sea ice observations and derived data. The spaceborne fully polarimetric C-band SAR data specifications, and the C-band SAR data and continent in-situ geophysical sampling regimes have been presented. The multiple steps of C-band SAR data processing have been described. Chapter four presents the implications of radar incidence angle.

Chapter Four

IMPLICATION OF THE RADAR INCIDENCE ANGLE

4.0 Introduction

The aim of this chapter is to discriminate FYI based on surface roughnesses which influences its C-band microwave scattering response during the late winter transition. Scattering from FYI is largely controlled by surface roughness but also by snow physical properties (moisture content, dielectric, etc), as a function of air temperature (Livingstone et al., 1987; Barber et al., 1995). This chapter partitions the FYI into three constituent scattering mechanisms on the basis of sea ice surface roughness: smooth ice (SI), rough ice (RI) and deformed ice (DI).

4.1 Visual Identification of the Three-Component Scattering Model over FYI

Figure 4.1-2 (a-d) visually illustrates the result of the three-component scattering mechanisms, contributions over snow covered FYI in Hudson Bay. The relative strength of the scattering mechanisms are presented in the false color composite images in Figure 4.1d and 4.2d, respectively for 39° and 29° incidence angles. Figures 4.1d and 4.2d show that blue color (surface scattering) dominated for all FYI types compared to the green and red where blue, green and red are contributed from surface, volume, and double-bounce scattering, respectively at 39° and 29° incidence angles.

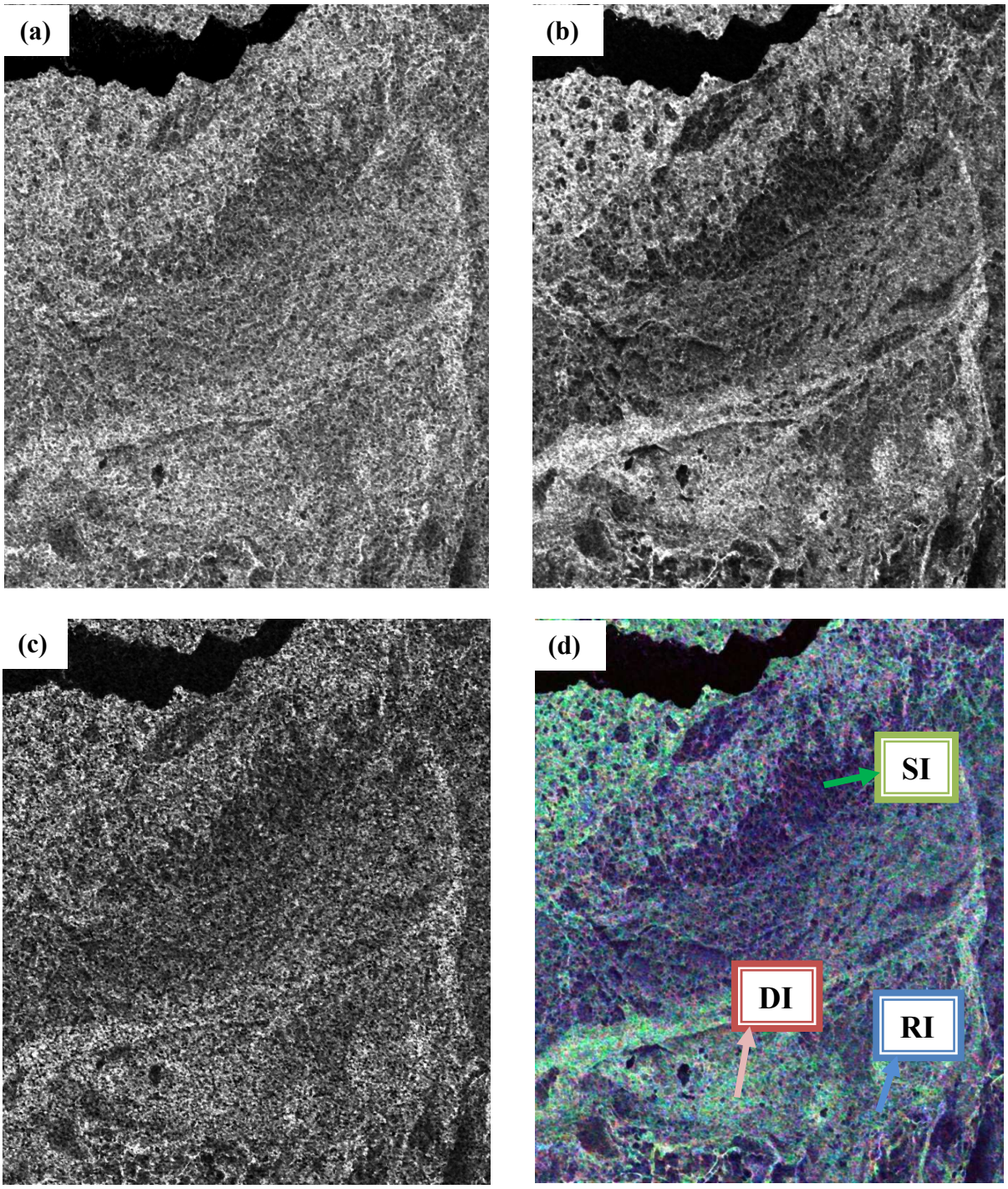

Figure 4.1: Visual display of three-component scattering model to decompose POLSAR C-band images over snow covered landfast FYI types: (a) Surface scattering, (b) Volume scattering, (c) Double-Bounce scattering, and (d) False color composite (R: Pd; G: Pv; B: Ps) images. Image acquired on May 15th, 2009 at 39° incidence angle.

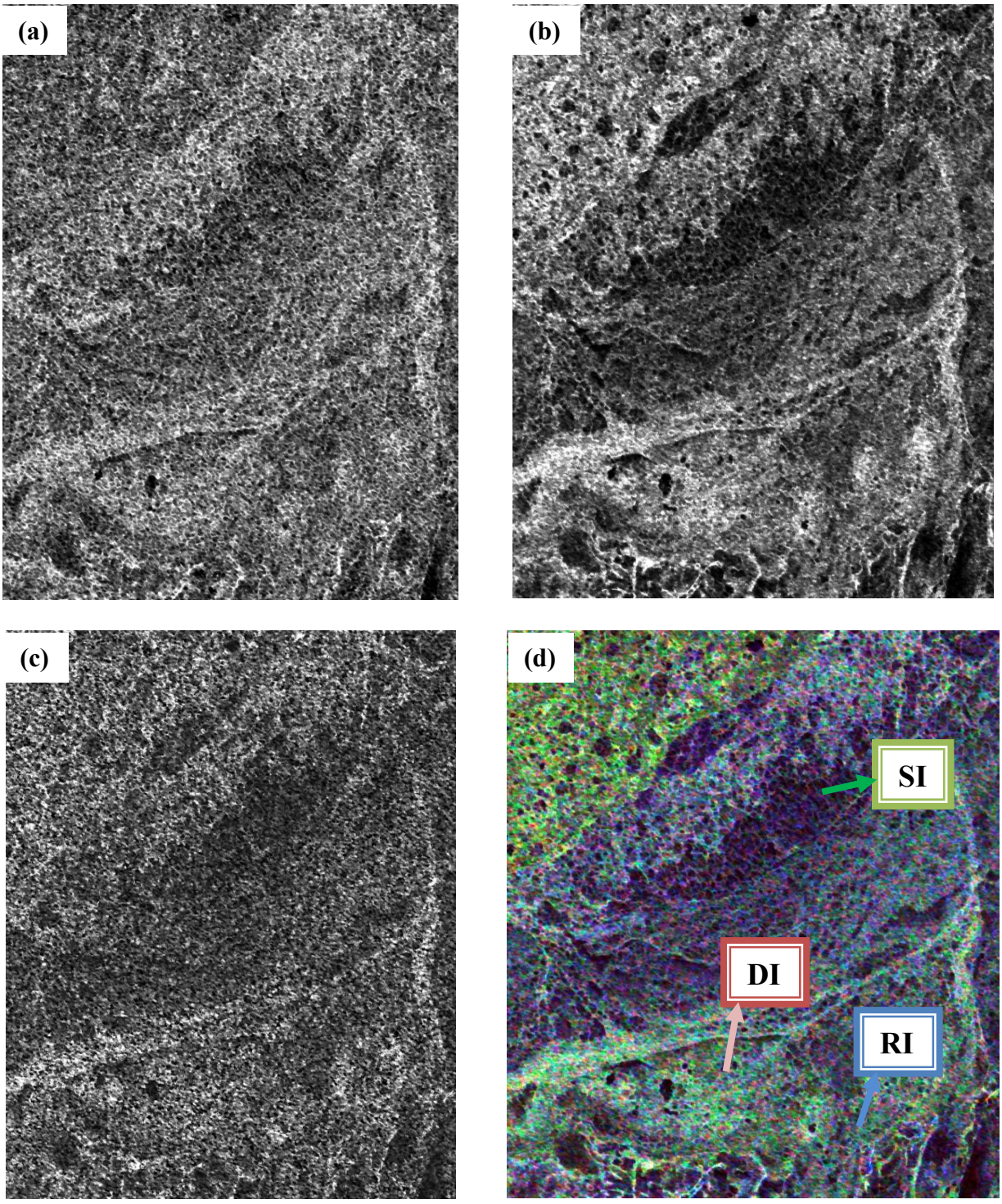

Figure 4.2: Visual display of three-component scattering model to decompose POLSAR C-band images over snow covered landfast FYI types: (a) Surface scattering, (b) Volume scattering, (c) Double-Bounce scattering, and (d) False color composite (R: Pd; G: Pv; B: Ps) images. Image acquired on May 18th, 2009 at 29° incidence angle.

4.2 Absolute Contributions of the Three-component Scattering Model over FYI

The absolute contributions to the three-component scattering mechanisms and total power signatures over snow covered FYI are illustrated in Figure 4.3. Backscatter from surface scattering is large compared to volume scattering for all three ice types but a negligible amount of scattering is measured from double-bounce scatterers (Figure 4.3b-d) which consistent with previous results (Scheuchl et al., 2002; 2005). However, at the steeper incidence angle (29°) higher backscatter values of surface (P_s), volume (P_v) and double-bounce (P_d) scattering are observed compared to the shallower (39°) incidence angle (Freeman and Durden, 1998). It is important to mention here that for smooth ice (SI) only, volume scattering is slightly higher at 39° (shallower) than 29° (steeper). I attribute this result to the shallower incidence angle microwave energy intercepting a greater volume of higher dielectric brine coated, enlarged snow grains in the basal layer compared to the case for the steeper incidence angle. An analogous situation occurs with atmospheric optical (mie) scattering that takes place during sunrises and sunsets due to the longer path length of the sunlight interacting with atmospheric particulates (red wavelengths scatterers).

Rough ice (RI) has a significant amount of volume scattering contribution to the total scattering, though surface scattering still plays a dominant role at both incidence angles (Figure 4.3b-d). Surface scattering has clear discrimination for RI at the two separate incidence angles when compared to volume and double-bounce scattering (Figure 4.3). Radar incidence angle has very little effect on volume scattering at about ≈ 1 dB for the incidence angle variation used here (Figure 4.3c) over snow covered FYI. This result suggests that one should use volume scattering parameters to separate FYI at different radar incidence angles. Double-bounce scattering from RI

shows larger scattering contribution than SI at the steeper incidence angle (Figure 4.3d) due to ice ridge occurrence and is consistent with previous results (Scheuchl et al., 2002; 2005).

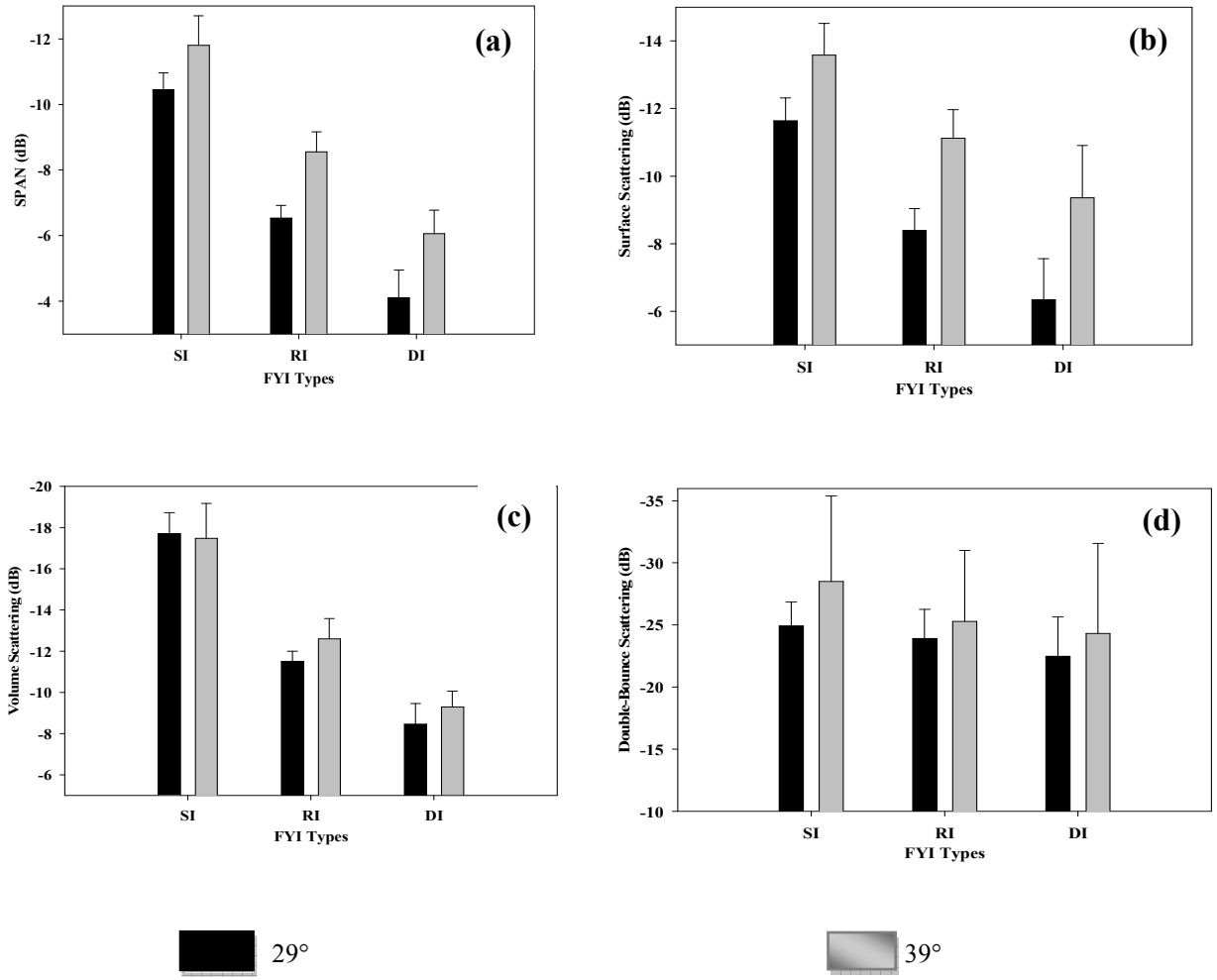

Figure 4.3: Three-component scattering mechanisms over snow-covered FYI at two incidence angles; 29° and 39°. X-axis contains FYI types (SI, RI and DI) and Y-axis contains (a) SPAN, (b) Surface scattering, (c) Volume scattering, and (d) Double-bounce scattering. The error bar shows the standard deviation of each class.

The results for deformed ice (DI) show that both surface and volume scattering are dominant when compared with SI and RI at the steeper incidence angle (Figure 4.3). The contributions of scattering mechanisms are higher at steeper incidence angles with mean differences ≈ 4 dB for P_s and ≈ 2 dB for P_v and P_d. The high amount of double-bounce

scattering observed from DI compared to RI and SI and is due to significant corner reflection from large ice ridges (Figure 4.3d). These results also agree with Scheuchl et al. (2002; 2005). The contribution of double-bounce scattering to total power increases with incidence angle and is due to higher reflected dihedral energy back to the radar sensor.

4.3 Microwave Backscatter Signatures

Figure 4.4 shows the microwave co- and cross-polarized backscatter coefficient signature over snow covered FYI at two separate incidence angles. The signature from co-polarized (σ^0_{xx} and σ^0_{yy}) channels (Figure 4.4a-b) depicts higher backscatter at the steeper incidence angle and it increases with surface roughness similar to previous results presented by Drinkwater et al., 1992; Nghiem et al., 1997 and Geldsetzer and Yackel, 2009. The cross-polarized (σ^0_{xy}) channel (Figure 4.4c) gives a low amount of backscatter as compared to the co-polarized channel and has less of a dependence on radar incidence angle than does the co-polarized channel. The value of σ^0_{xy} increases with surface roughness and decreases with incidence angle except for SI where σ^0_{xy} is higher at the shallower angle compared to the steeper incidence angle (Figure 4.4c). This result again suggests that enhanced volume scattering is occurring for SI targets whereby enlarged, brine coated snow grains in the basal snow layer have an increased total scattering contribution (i.e. cross-section) at the shallower incidence angle (i.e. sunrise/sunset effect) (Yackel and Barber, 2007; Barber and Nghiem, 1999).

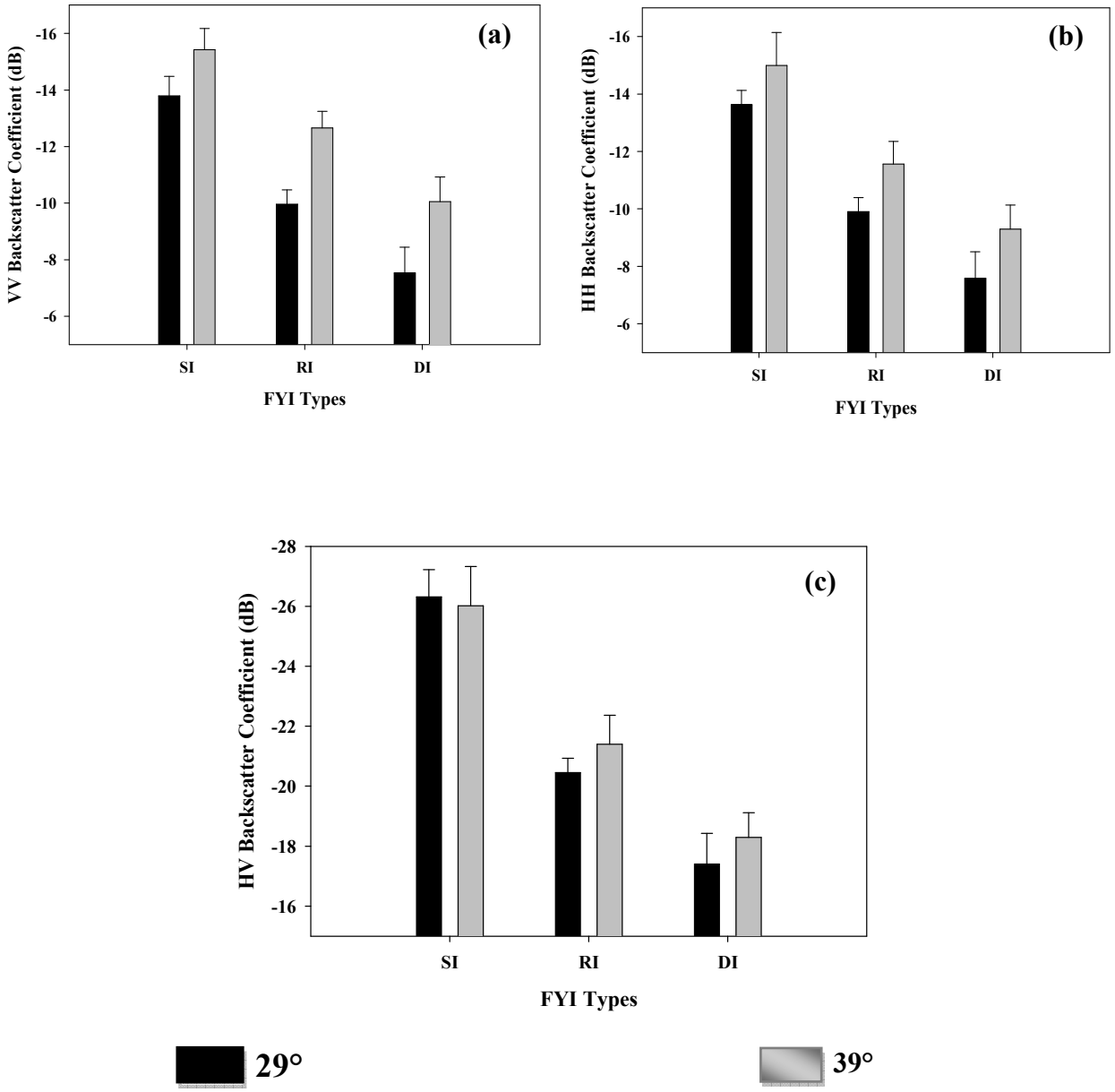

Figure 4.4: Microwave backscatter at co- and cross-polarized channels over snow-covered FYI. X-axis contains FYI types and Y-axis represents (a) VV, (b) HH, (c) HV. The bar charts are mean values of 200 samples in each class and error bars represent standard deviation.

The co-polarized ratio (γ_{co}) is higher at 39° which increases with increasing surface roughness and has more discrimination between ice types at shallower incidence angles when compared to steeper incidence angles (Figure 4.5a). γ_{co} tends to approach zero or becomes negative as the surface becomes rougher. This can be due to Fresnel reflection effects (a phenomenon related to line of sight whereby an object that does not obstruct the visual line of sight obstructs the line of transmission for radio frequencies) from the specular ice surface which has an enhanced effect at shallower incidence angles (Walter et al., 2008). This result is consistent with previous studies by Drinkwater et al., (1992); Drinking and Askane (1998); and Geldsetzer and Yackel, (2009).

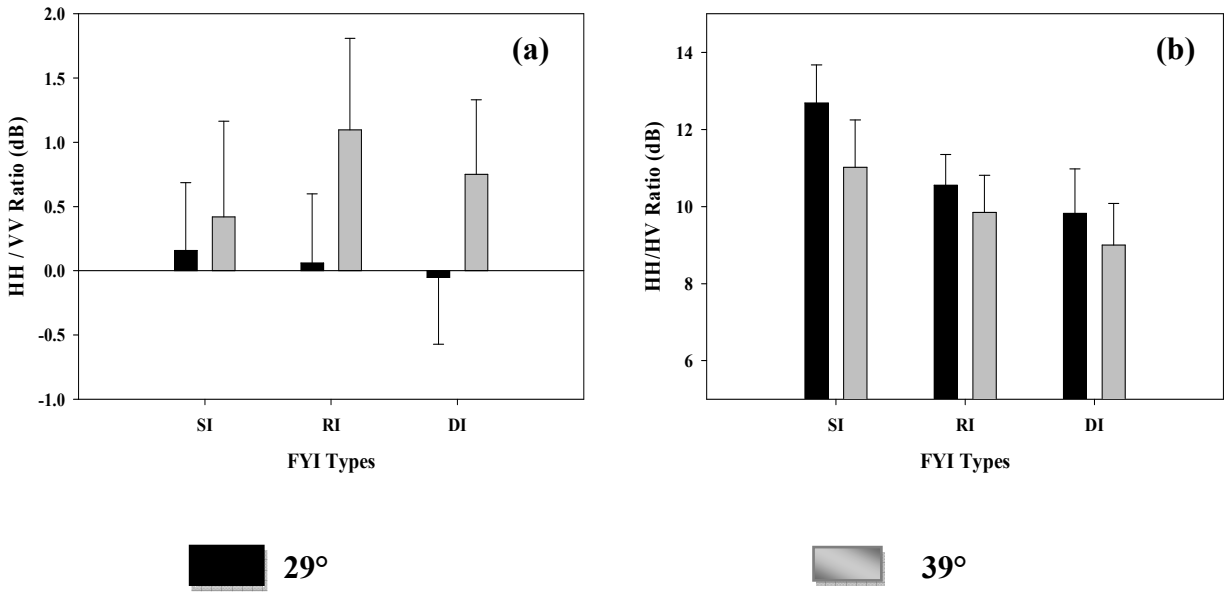

Figure 4.5: Microwave backscatter at co- and cross-polarized channels over snow-covered FYI. X-axis contains FYI types and Y-axis represents (a) HH/VV ratio, and (b) HH/HV ratio. The bar charts are mean values of 200 samples in each class and error bars represent standard deviation.

The cross-polarized backscatter ratio (γ_{cr}) is higher at the steeper incidence angle (Figure 4.5b) for all ice types but highest for SI (Figure 4.5b) as a result of the increase in specular scattering from SI at HH (Freeman and Durden, 1998). This cross-polarized value decreases with increasing surface roughness (Figure 4.5b).

4.4 Polarimetric Radar Parameters

Entropy (H) is found to be higher at the shallower incidence angle compared to the steeper incidence angle and increases with surface roughness (Figure 4.6a). This result is likely attributable to the fact that shallower incidence microwave energy has greater contact with the snow volume compared to the steeper incidence angle. This result suggests that the number of important scattering mechanisms increases with increasing surface roughness (Cloude and Pottier 1997; Cloude and Papathanassiou, 1999).

Anisotropy (A) is highest for SI and it decreases with surface roughness (Figure 4.6b) which can be due to the presence of random scattering. The higher value of A for SI observed at the steeper incidence angle compared to the shallower incidence angle (Figure 4.6b) corroborates previous observations and explains an increased scattering cross-section from volume scatterers within the snow cover. The value of A for SI indicates the presence of multiple scattering from within the snow cover (Cloude and Papathanassiou, 1999). Alpha angle (α) identifies the dominant scattering mechanism present in the object. Lower magnitude alpha angle values indicate that surface scattering is dominant. Moderate magnitudes indicate that volume scattering makes a significant contribution and a high value indicates the presence of double-bounce scattering (Cloude and Pottier, 1997). Values of α here suggest that surface scattering is dominant. The higher magnitude of α consistently observed at the shallower incidence angle can

again be attributed to microwave energy being in greater cross-sectional contact with the higher dielectric basal snow layer (Figure 4.6c).

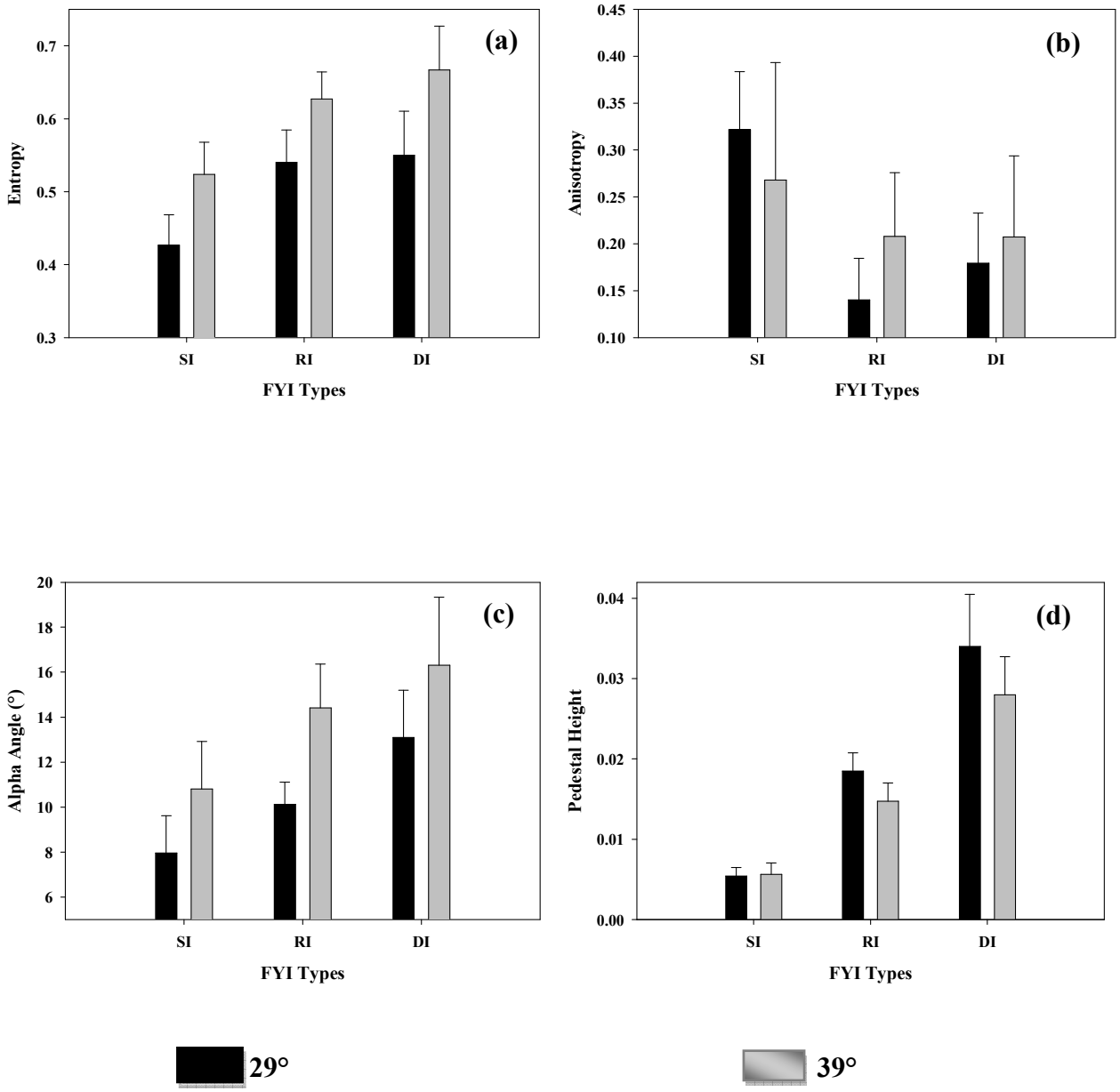

Figure 4.6: Selected polarimetric backscatter parameters for ice types at 29° and 39° incidence angles. X-axis contains FYI types and Y-axis represents (a) Entropy, (b) Anisotropy, (c) Alpha angle, (d) Pedestal height. The black and grey solid bar represents the mean sample values at 29° and 39° incidence angle respectively. The error bars represent the standard deviation of each class.

The pedestal height (P) indicates the presence of un-polarized scattering components and assists in depicting the type of scattering mechanisms (Evans et al., 1988). The value of P increases with surface roughness at both incidence angles. Radar incidence angle has no significant effect on P for SI (Figure 4.6d). Higher P values are found at the steeper incidence angle for the rougher ice types.

The co-polarized phase differences (ϕ_{xx-yy}) are used to discriminate groups of pixels on the basis of electromagnetic radar signal interactions of objects. The lower magnitude of φ_{xx-yy} value indicates the object is smooth and it increases with surface roughness (Winebrenner et al., 1995). Higher (φ_{xx-yy}) values are observed at shallower angles and lower values at our steeper incidence angles except for RI (Figure 4.7a). This is likely due to the random orientation of surface roughness features (i.e. randomly oriented ice blocks/fragments) on RI.

The co-polarized correlation coefficient of variation (μ_{xxyy}) is used for discriminating surface properties and characterizes homogeneous areas in SAR images (d'Alvise et al., 1999). The results presented here show higher values at the shallower angle and lower at the steeper incidence angle with the value increasing with surface roughness at both incidence angles (Figure 4.7b).

Fractional power is higher at the steeper incidence angle and lower at the shallower incidence angle. This value decreases with increasing surface roughness and can be due to random orientation of RI and DI features (Figure 4.7c). This indicates surface scattering is dominant on SI and decreases with the increasingly heterogeneous nature of ice deformation and roughness features.

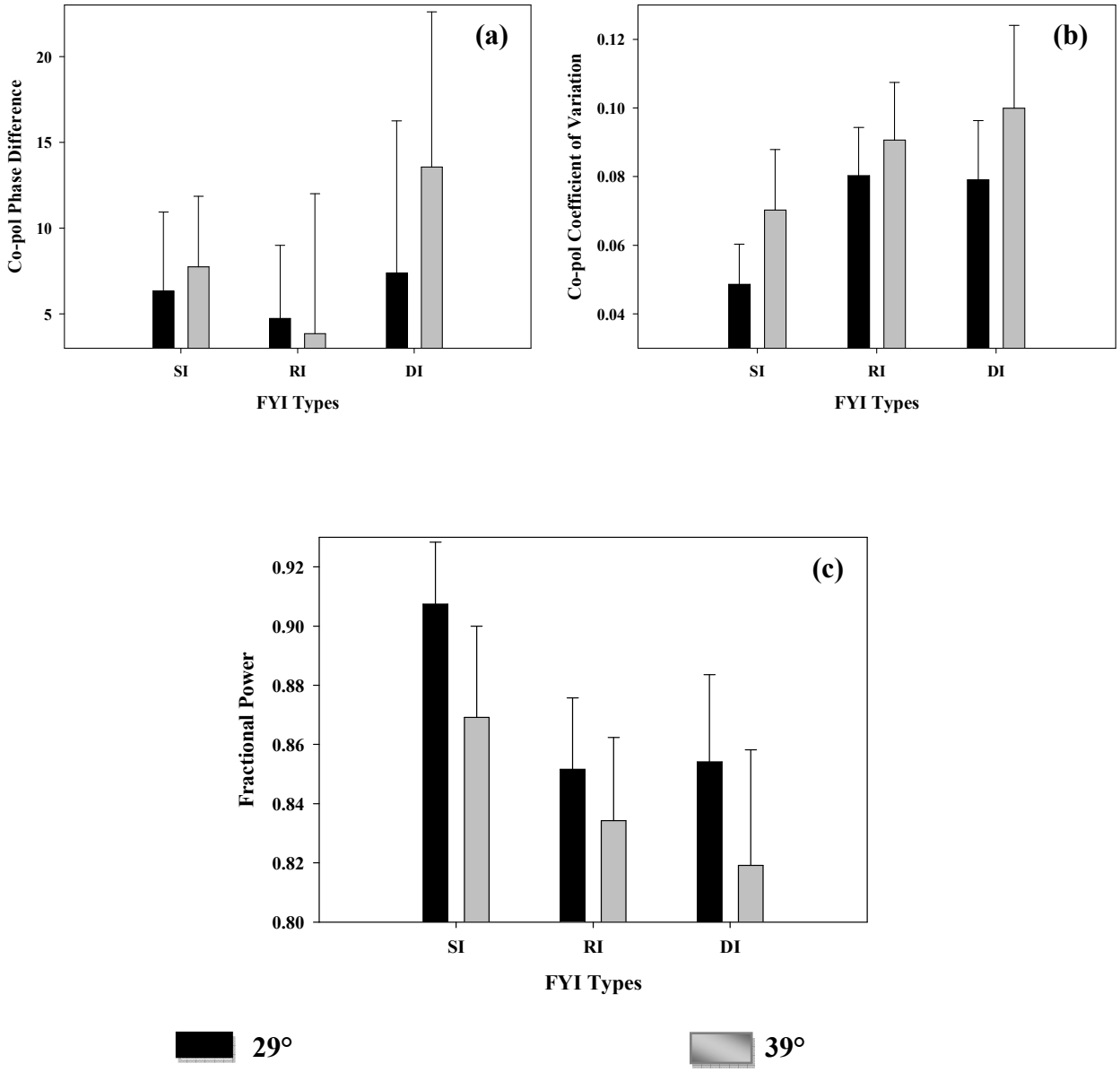

Figure 4.7: Selected polarimetric backscatter parameters for ice types at 29° and 39° incidence angles. X-axis contains FYI types and Y-axis represents (a) Co-pol phase difference, (b) Co-pol coefficient of variation, (c) Fractional power. The black and grey solid bar represents the mean sample values at 29° and 39° incidence angle respectively. The error bars represent the standard deviation of each class.

4.5 Three-component Scattering Model for Discriminating FYI types

Figures 4.8 and 4.9 (a-b) illustrate the ability of the three-component scattering model to discriminate snow covered FYI types by separating the proportional scattering contributions at two different incidence angles. Figure 4.8a illustrates the separation of three different FYI types using the contributions of Pv and Pd at 29° and 39° incidence angles, respectively. Significant discrimination between different FYI types is also observed between Ps and Pv in (Figure 4.8b). The proportional contribution of Ps versus Pd is able to discriminate SI at 29° but at 39° it involves some ambiguities between RI and DI (Figure 4.9a). Improved discrimination is visually observed in Figure 4.9b using a third axis where all three scattering contributions (Ps, Pd and Pv) are compared at the two different incidence angles. The steeper incidence angle shows a higher magnitude of those three scattering contribution compared to shallower incidence angle and plays a significant role in discriminating FYI types.

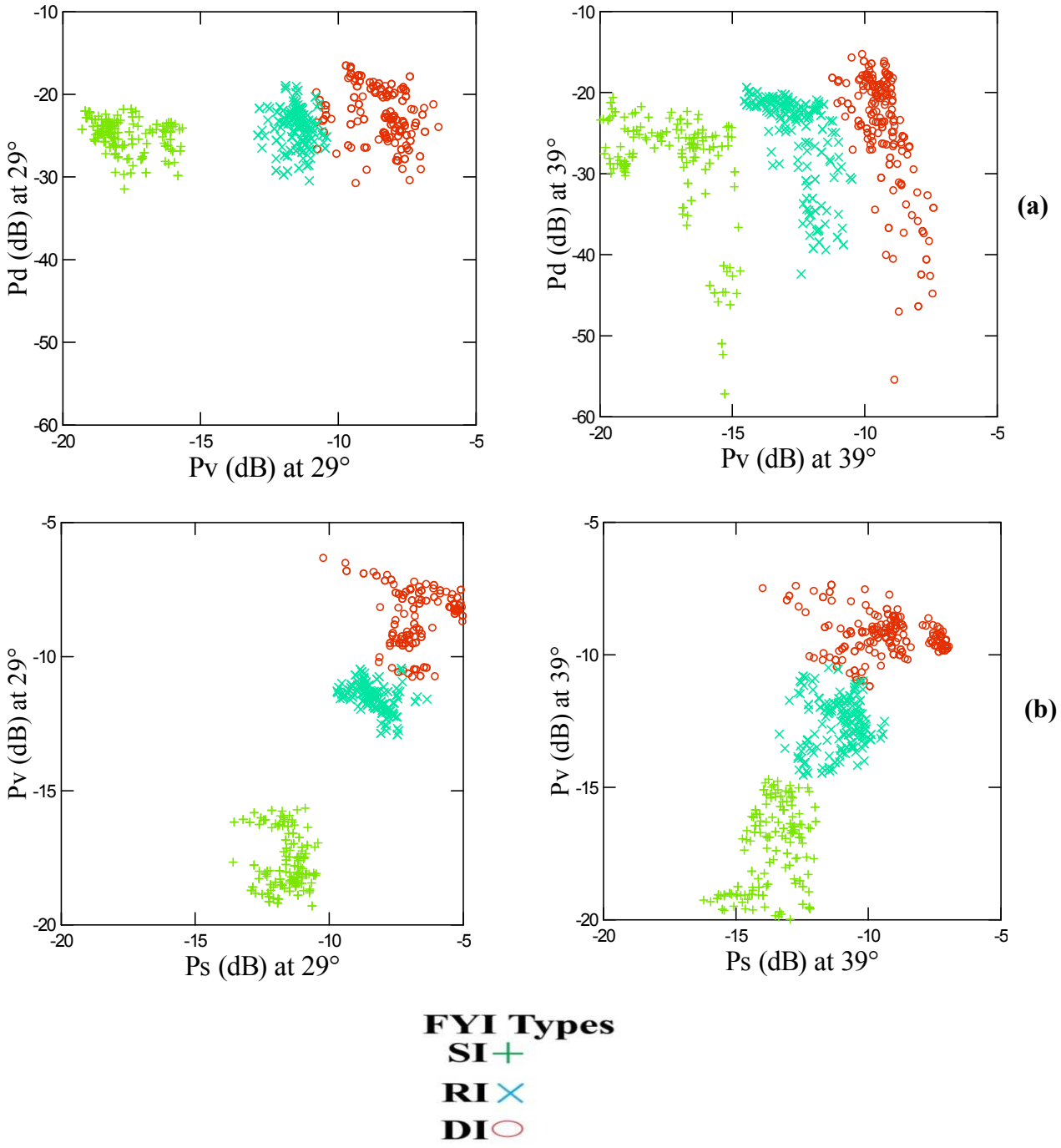

Figure 4.8: Visual discrimination of snow covered FYI types (a) X-axis contains volume scattering (P_v) and Y-axis contains double-bounce scattering (P_d) for both at 29° and 39°; (b) X-axis contains surface scattering (P_s) and Y-axis contains P_v for both at 29° and 39° incidence angle respectively. The green, cyan and red color represents SI, RI and DI respectively.

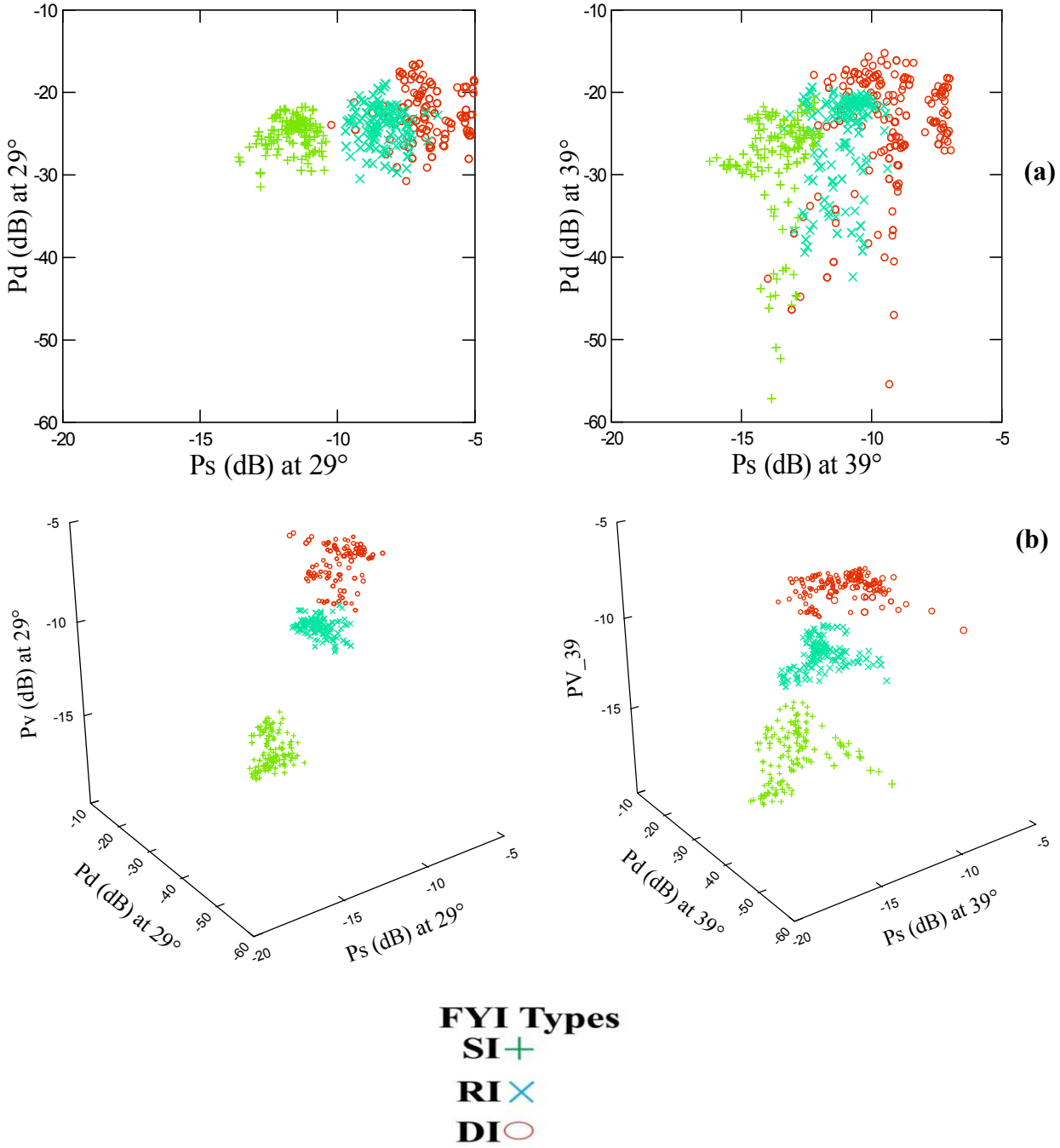

Figure 4.9: Visual discrimination of snow covered FYI types (a) X- axis contains P_s and Y-axis contains P_d for both at 29° and 39° incidence angle respectively; and (b) 3-D illustrations provide X-axis P_s, Y-axis P_d and Z-axis Pv for both 29° and 39° incidence angle accordingly. The green, cyan and red color represents SI, RI and DI respectively.

4.6 Proportional Contribution of the Three-Component Scattering Model

The quantitative proportional contributions of the three-component scattering model over snow covered FYI types at the two specific radar incidence angles is presented in Table 4.1.

Table 4.1: The proportional contribution of the three-component scattering model over snow covered FYI types at two radar incidence angles.

Incidence Angle (°)	FYI Types	P_s (%)	P_d (%)	P_v (%)	Total
29°	SI	77.27	03.63	19.09	100
	RI	65.97	01.85	32.18	100
	DI	61.09	01.48	37.43	100
39°	SI	69.48	02.23	28.29	100
	RI	57.13	02.19	40.68	100
	DI	48.99	01.56	49.54	100

Ps decreases with increasing radar incidence angle and surface roughness. It decreases approximately 8% for SI and RI and ~ 12% for DI over our 10° incidence angle range. P_d exhibits low magnitude scattering contributions for both incidence angles and contributes a nearly negligible amount to the total scattering power. A higher value of P_d is measured for SI at the steeper incidence angle and for RI and DI at shallower incidence angles. SI contributes a slightly higher amount of P_d at 29° and decreasing ~ 1.4% over the 10° incidence angle range. P_v is the second dominant scattering mechanism over snow covered FYI types and it increases with surface roughness as well as radar incidence angle. The higher amount of P_v measured for

rougher ice types and lower amount for SI at both incidence angles agrees with microwave interaction theory and previous results. It is found that P_s and P_v has a similar effect on radar incidence angle dependence for different FYI types.

4.7 Summary

Section 4.1 has described the results of visual identification of three simple scattering mechanisms over snow covered FYI at two specific incidence angles. The results indicate that surface scattering is dominated for all three FYI types (SI, RI and DI) at both incidence angles. Section 4.2 has presented the results of absolute contribution of three simple scattering mechanisms over FYI at 29° and 39° incidence angles. The results also indicate that higher scattering mechanisms are measured at 29° compared to 39° for FYI types except for SI whereas in volume scattering is slightly higher at 39° compared to 29°. These differences are evident in the cross-polarization backscattering in the section 4.3. A subsequent increase in volume and cross-polarization backscattering signatures is caused by increasing greater contact with brine basal layer at 39° compared to 29°. Section 4.4 has described the results of polarimetric SAR parameters signatures over snow covered FYI types at two incidence angles. The results indicate that signature influences with radar incidence angles as well as degree of surface roughness except for SI in pedestal height. These results indicate that pedestal height can be useful for SI separation at different incidence angles. Section 4.5 has presented the results of three-component scattering model and their ability for discriminating FYI types at two specific incidence angles (29° and 39°). The results show that three-component scattering model is able to discriminate FYI types at 39° incidence angle compared to 29° by using both 2-D and 3-D plot. Section 4.6 has described the proportional contribution of the three-component scattering

model over FYI types. The results indicate that P_s decreases with surface roughness as well as increasing incidence angle, on the other hand P_v increases with roughness as well as increasing with radar incidence angle. Chapter five presents polarimetric signatures at heterogeneous snow cover over smooth FYI.

Chapter Five

OBSERVATIONS OF SNOW COVER DISTRIBUTION

5. Introduction

In this chapter, the potential of fully polarimetric C-band SAR for improved snow water equivalent retrieval during the late winter transition over smooth first-year sea ice (SFYI) is evaluated. Two climatic regimes, polarimetric C-band SAR parameters and a three-component scattering model have demonstrated utility in estimating snow cover distribution - thin, medium and thick snow cover- which has advanced our understanding of snow cover distribution over FYI within the broader climate system (Drobot and Anderson, 2001; Howell et al., 2005; Yackel et al., 2007; Yackel and Barber, 2007).

5.0 Significance Test of the Snow Thickness Sampling Site

The output of an ANOVA test for each snow thickness class test site is given in Table 5.1 (a-b) and Table 5.2 (a-b). P values less than 0.05 indicate a significant difference among the three sub-groups which contain 613 pixel samples for each snow thickness class. Results from this test suggest (Table 5.1a) considerably more within-site variability for thicker snow areas on SFYI at cold air/snow surface temperatures compared to thinnest snow covers. The opposite was observed for warmer cases where more variation was measured for thin snow cover SFYI as compared to thicker snow covered SFYI.

Table 5.1 (a): ANOVA p-value's for within-class variation of C-band polarimetric parameters for each snow thickness class at −8.0° C. P-values in bold (< 0.05) indicate a significant difference among the 3 within-site samples for each snow thickness class.

POLSAR\Classes	P-Values			
	Thin	Medium1	Medium2	Thick
HH	0.862	**0.006**	0.363	**0.000**
VV	0.729	**0.004**	0.459	**1.8E-07**
HV	0.461	**3.9E-06**	0.182	**3.3E-05**
HH-VV	0.076	0.229	0.976	0.114
HH-HV	0.818	**0.017**	0.336	**0.002**
Ps	0.391	0.704	0.076	**0.004**
Pv	0.019	0.178	**0.008**	**3.5E-05**
Pd	0.931	0.706	**0.005**	0.754
Ps-Pv	0.339	0.861	0.408	0.746
TP	0.346	0.495	0.487	**1.4E-07**
H	0.475	**0.049**	0.449	0.118
A	0.118	0.088	0.512	0.302
Alpha	0.376	0.772	0.213	0.847

Table 5.1 (b): ANOVA p-value's for within-class variation of C-band polarimetric parameters for each snow thickness class at −0.4° C. P-values in bold (< 0.05) indicate a significant difference among the 3 within-site samples for each snow thickness class.

POLSAR\Classes	P-Values			
	Thin	Medium1	Medium2	Thick
HH	0.332	0.607	0.832	0.316
VV	0.952	0.764	0.462	0.355
HV	**4.3E-21**	**0.001**	0.194	0.618
HH-VV	**0.039**	0.584	0.409	0.056
HH-HV	0.192	0.760	0.803	0.359
Ps	0.123	0.769	0.297	0.248
Pv	**2.6E-21**	0.409	0.965	0.095
Pd	0.466	**8.2E-06**	0.582	0.769
Ps-Pv	0.804	0.885	0.126	0.356
TP	0.829	0.592	0.693	0.296
H	**6.6E-12**	0.474	**5.4E-07**	**0.015**
A	**0.017**	**4.5E-06**	0.777	**0.001**
Alpha	**1.0E-14**	0.174	0.278	**0.003**

This study argues that, for the cold case, the large standard deviation in snow thickness measured at the thick site (19.8 cm; Table 3.3) produces considerable backscattering variability considering that the snow thickness sampling scale (1 m) approaches that of individual SAR

pixels (5 m). As a result, considerable variation is expected in snow volume and ice surface brine volume and subsequent dielectric properties from the thin snow site compared to the thick snow site for the warm case. This preliminary analysis suggests that simple co-pol measures (ie. HH and VV) are more sensitive to within-site snow thickness variability at colder air/snow ice interface temperatures compared to the warmer case. However, in general, this analysis suggests that each of the four sites exhibits homogeneous snow thickness for most of the POLSAR measures used in the study.

Table 5.2 (a): ANOVA result for between-class variation of C-band polarimetric parameters at −8.0° C. P-values in bold (< 0.05) indicate a significant difference between snow thickness classes.

POLSAR\Classes	P-Values					
	ThnVsMed1	ThnVsMed2	ThnVsThk	Med1VsThk	Med2VsThk	Med1VsMed2
HH	**0**	**0**	**0**	**0**	**0**	**1.7E-4**
VV	**0**	**0**	**0**	**0**	**0**	**0.045**
HV	**2.7E-9**	**0**	**0**	**0**	**0**	**8.8E-3**
HH-VV	**1.2E-2**	**1.9E-1**	0.371	**0.001**	0.433	**1.2E-1**
HH-HV	**0**	**0**	**0**	**0**	**0**	**5.5E-3**
Ps	**0**	**0**	**0**	**0**	**0**	**0.039**
Pv	**0**	**0**	**0**	**0**	**0**	**8.9E-3**
Pd	**0**	**0**	**3.6E-2**	**0**	**0**	0.289
Ps-Pv	**0**	**0**	**0**	**0**	**0**	**0.002**
TP	**0**	**0**	**0**	**0**	**0**	**7.7E-2**
H	**0**	**3E-7**	**0**	**4.1E-3**	**0**	**5.8E-2**
A	**1.2E-3**	**8.1E-3**	**0**	**0**	**0**	**0.001**
Alpha	**7.3E-3**	**0**	**0**	**6.5E-3**	**1.7E-1**	**8.5E-5**

Table 5.2 (a-b) shows pairwise comparison between the four snow thickness classes. The p-value is the probability of concluding that there is a significance statistical difference between the snow thickness classes. Significant differences are found except for a few parameters whose p-values are highlighted in bold color.

Table 5.2 (b): ANOVA result for between-class variation of C-band polarimetric parameters at −0.4°C. P-values in bold (<0.05) indicate a significant difference between snow thickness classes.

POLSAR\Classes	P-Values					
	ThnVsMed1	ThnVsMed2	ThnVsThk	Med1VsThk	Med2VsThk	Med1VsMed2
HH	**0**	**0**	**4.2E-5**	**0**	**0**	**3.3E-8**
VV	**0**	**0**	**7.8E-8**	**0**	**0**	**6.6E-9**
HV	**0**	**0**	**4.2E-1**	**0**	**0**	**0**
HH-VV	**1.7E-4**	**3.7E-3**	**1.5E-2**	**0.008**	**0.024**	0.754
HH-HV	**0**	**0**	**4.0E-5**	**0**	**0**	**5.6E-6**
Ps	**0**	**0**	**3.3E-7**	**0**	**0**	**1.8E-5**
Pv	**0**	**0**	0.145	**0**	**0**	**0**
Pd	**8.1E-3**	**2.8E-2**	**1.4E-7**	**1.7E-6**	**3.6E-4**	**7.6E-1**
Ps-Pv	**0**	**0**	**4.6E-7**	**3.5E-3**	**2.8E-2**	**5.9E-1**
TP	**0**	**0**	**4.7E-7**	**0**	**0**	**1E-1**
H	**0**	**1.5E-5**	**6.1E-2**	**0**	**1E-1**	**2E-3**
A	**2.4E-3**	**5.2E-4**	**5.4E-1**	**1.9E-2**	**2.3E-2**	**1E-1**
Alpha	**5.5E-9**	**1.9E-2**	**2E-1**	**0**	**1.3E-4**	**6E-2**

5.1 Absolute Contributions of the Three-Component Scattering Model

The absolute contributions of the three-component scattering mechanisms on different snow thickness classes over SFYI are illustrated in Figure 5.1. It is observed that surface scattering (P_s) contributes significantly more to the total scattering compared to volume (P_v) and double-bounce (P_d) scattering for all snow classes at two different air and snow surface temperatures. P_s and P_v have been the first and second important scattering mechanism and P_d has a very negligible contribution to the total scattering over snow covered FYI. Higher values of P_s are measured for warm cases for all snow thickness classes compared to cold cases and significant variation is observed at thin classes compared to the others (Figure 5.1a). This change can be due to the aforementioned thermodynamic effect of SWE whereby the thinnest snow permitted the largest amount of temperature change at the snow-ice interface (Table 3.3) causing a larger dielectric change and subsequent change in scattering compared to thicker snow classes.

The magnitude of P_s decreases with increasing snow thickness until the medium2 (21 cm) snow class, then it increases again with thicker (36 cm) snow (Figure 5.1a) and shows similar magnitudes for both cases (Cold-Warm). P_v is higher for warm conditions compared to cold cases for three of the four snow thickness classes over SFYI except for the thickest class (Figure 5.1a). These results can be due to the SAT effect on the snow sites (Figure 3.5 and Table 3.3) whereby the thinnest snow permitted a quick response from the SAT forcing to the basal layer of the snow compared to thicker snow covers. The result is to force an increase in basal layer brine volume and cause an increase in the dielectric permittivity. P_d makes very little contribution to the total scattering for all four snow thickness classes at two different climatic cases (Figure 5.1a). It shows that Pd decreases with increasing snow thickness until medium2, then contributes higher values at thicker snow covers (Figure 5.1a). P_d has very little sensitivity to SAT/sea-ice interface temperature (only ~ 0.4 dB variation) for the thick snow class, which can be used to discriminate the thicker snow class over SFYI.

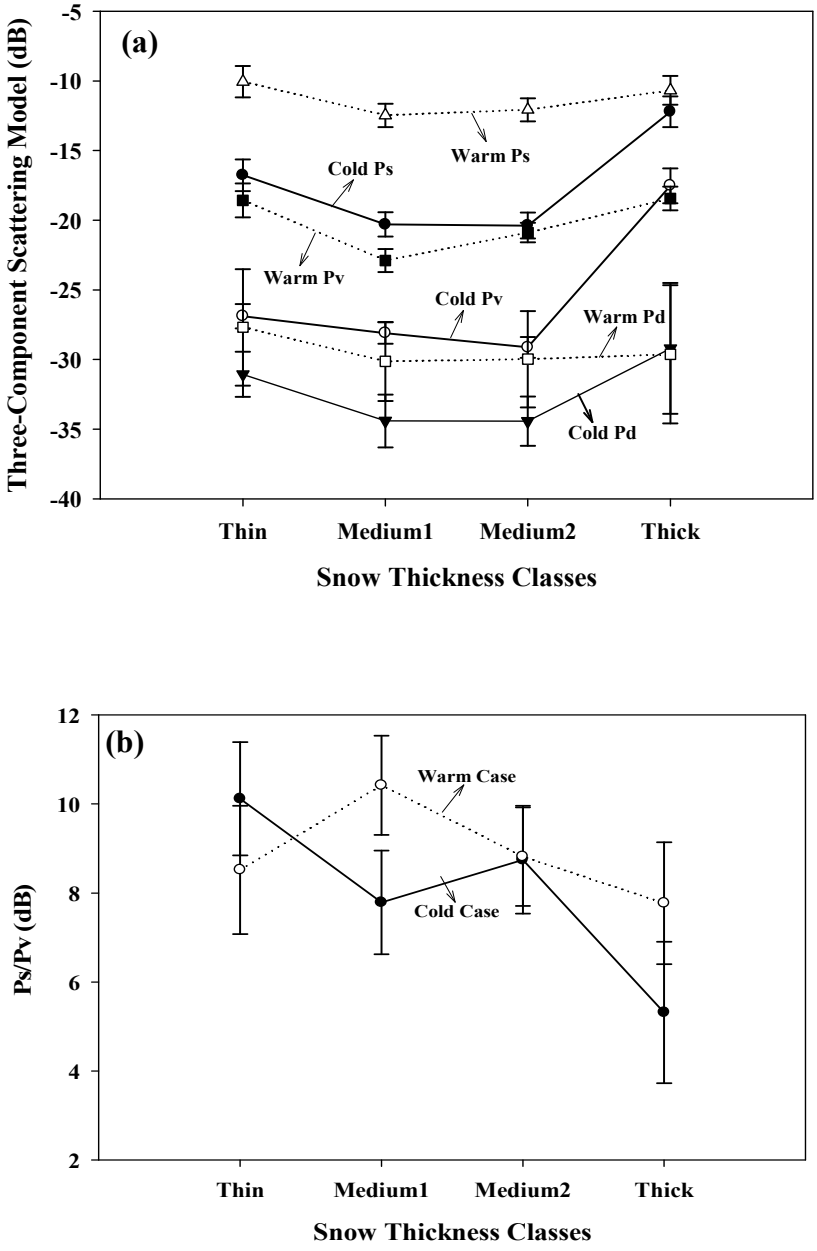

Figure 5.1: Absolute contribution of the three component scattering model over snow covered SFYI at two different surface air temperature conditions. X-axis contains snow thickness classes (Thin, Medium1, Medium2 and Thick) and Y-axis contains (a) Three component scattering model (Surface scattering, P_s; Volume scattering, P_v; and Double-Bounce scattering, P_d; and (b) P_s/P_v. The error bars show the standard deviation of each class.

The absolute variation of the P_s/P_v ratio on four different snow thickness classes over SFYI is illustrated in Figure 5.1b. There are absolute scattering variations from P_s to P_v indicating 5.3 dB higher for the cold case and 7.8 dB lower for the warm case for the thicker snow class, indicating a strong P_v scattering component for cold cases which can be due to SAT forcing from the previous day. Thin snow cover shows 10 dB and 8.5 dB difference between P_s and P_v for cold and warm cases respectively, indicating that P_v increases at warmer SAT's due to a thermodynamic effect (Barber and Thomas, 1998; Yackel and Barber, 2007).

5.2 Microwave Backscatter Signatures

$SPAN$ shows higher magnitude of microwave backscatter for the warm case for all snow thickness classes compared to the cold case (Figure 5.2a). Significant variation in $SPAN$ is observed for thin and thick snow classes at for two climatic conditions. Higher $SPAN$ is observed for the thin snow class for both climatic conditions. This result can be due to the thermodynamic effect which produces larger backscattering from the ice layer, brine coated layer and snow grains. The thick snow class produces higher $SPAN$ values (Figure 5.2a) for the cold case, indicating the effect of earlier days, SAT (Figure 3.6).

The microwave co- and cross-polarized backscatter coefficient signature over snow covered SFYI at for two climatic regimes is illustrated in Figure 5.2b. The signature from the co-polarized (σ^0_{xx} σ^0_{xx} and σ^0_{yy} σ^0_{yy}) channel depicts higher backscatter values for the warmer climatic regime and it decreases with increasing snow thickness until medium2, then it increases for the thick snow class. These results can be due to lack of microwave energy penetration through the snow cover and the thermodynamic effect on snow and snow-ice interface layer. This corroborates previous studies (Barber and Nghiem, 1999; Yackel and Barber, 2007). The cross-

polarized (σ^0_{xy}) channel (Figure 5.2b) gives lower microwave backscatter as compared to the co-polarized channel and is less sensitive to snow thickness for thin-medium2 classes for the cold cases. The higher magnitude of σ^0_{xy} measured at thick snow cover for cold cases −26.3 dB (and −27.2 dB for warm cases), indicates less effect on SAT. There are −7.2 and 0.9 dB variations between thin and thick snow classes for two climatic regimes, depicting a strong thermodynamic effect on thin snow compared to thick snow. This was a result of an increased microwave penetration through the thin snow (Barber and Nghiem, 1999; Yackel and Barber, 2007).

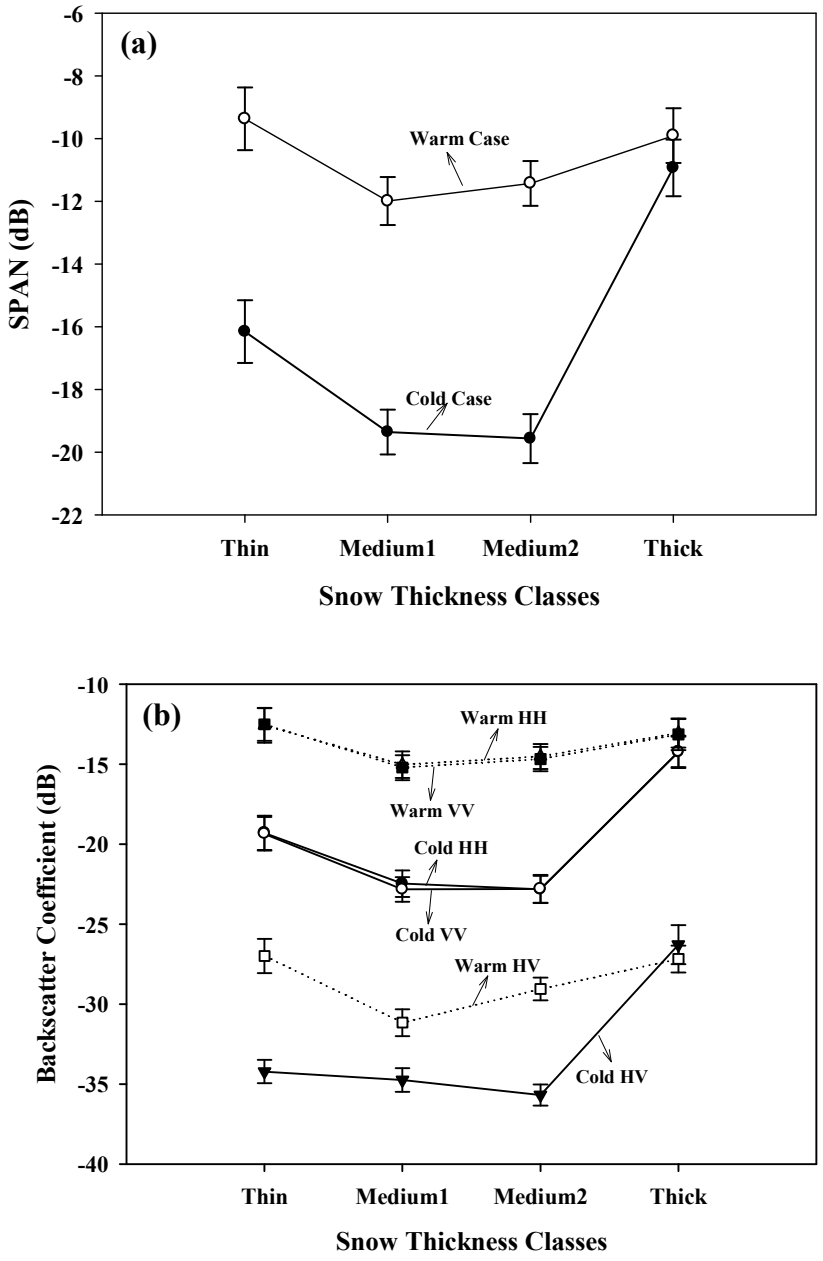

Figure 5.2: Microwave backscatter signatures at co and cross-polarized channels over snow covered SFYI. X-axis contains snow thickness classes and Y-axis represents (a)$SPAN$; and (b) Backscatter Coefficient (HH, VV, and HV). The points represent mean values of 1839 sample pixels in each class and error bars represents standard deviation.

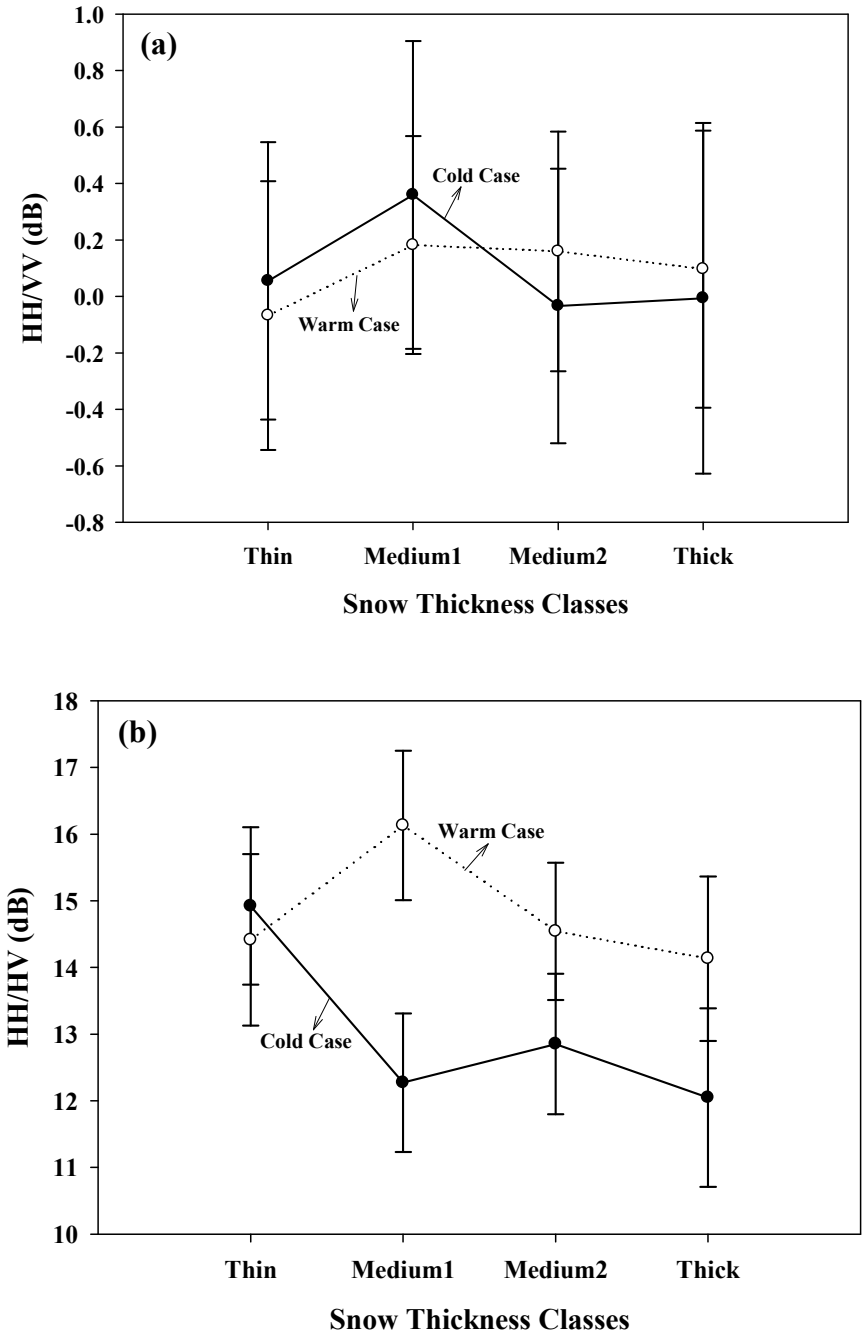

Figure 5.3: Microwave backscatter signatures at co and cross-polarized channels over snow covered SFYI. X-axis contains snow thickness classes and Y-axis represents (a) HH/VV, and (b) HH/HV. The point represents mean values of 1839 sample pixels in each class and error bars represents standard deviation.

The results again suggest that an increase in volume scattering is occurring for thin and thick snow whereby enlarged, brine coated snow grains in the basal snow layer have a significant total scattering contribution (Yackel and Barber, 2007; Barber and Nghiem, 1999).

The co-polarized ratio (γ_{co}) is higher for the warm case and lower for the cold case except for thin and medium1 classes and it increases with increasing snow thickness up to snow class medium1 then decreases again for medium2 and thick snow classes (Figure 5.3a). γ_{co} tends to approach zero or negative for thicker snow for the cold case and for thin snow for the warm case. This can be due to Fresnel reflection effects from the specular ice surface. The cross-polarized backscatter ratio is higher for the thin and medium1 snow classes for the cold and warm cases respectively and lower for thicker snow class for both climatic regimes (Figure 5.3b). This is mostly likely a result of the dominant surface backscattering for the thin snow cover case compared to thick snow cover. This cross-polarized value decreases with increasing snow thickness (Figure 5.3b).

5.3 Polarimetric Target Decomposition Parameters

Entropy (H) is found to be higher over thick snow cover compared to other snow classes for both climatic regimes and it increases with increasing snow thickness except for medium1 and medium2 for the warm and cold cases respectively (Figure 5.4a). This result suggests that the microwave energy interacts with snow grain size, density, and brine coated layers within the thicker snow cover. This result also suggests that the number of dominant scattering mechanisms increases with increasing snow thickness (Cloude and Pottier 1997; Cloude and Papathanassiou, 1999).

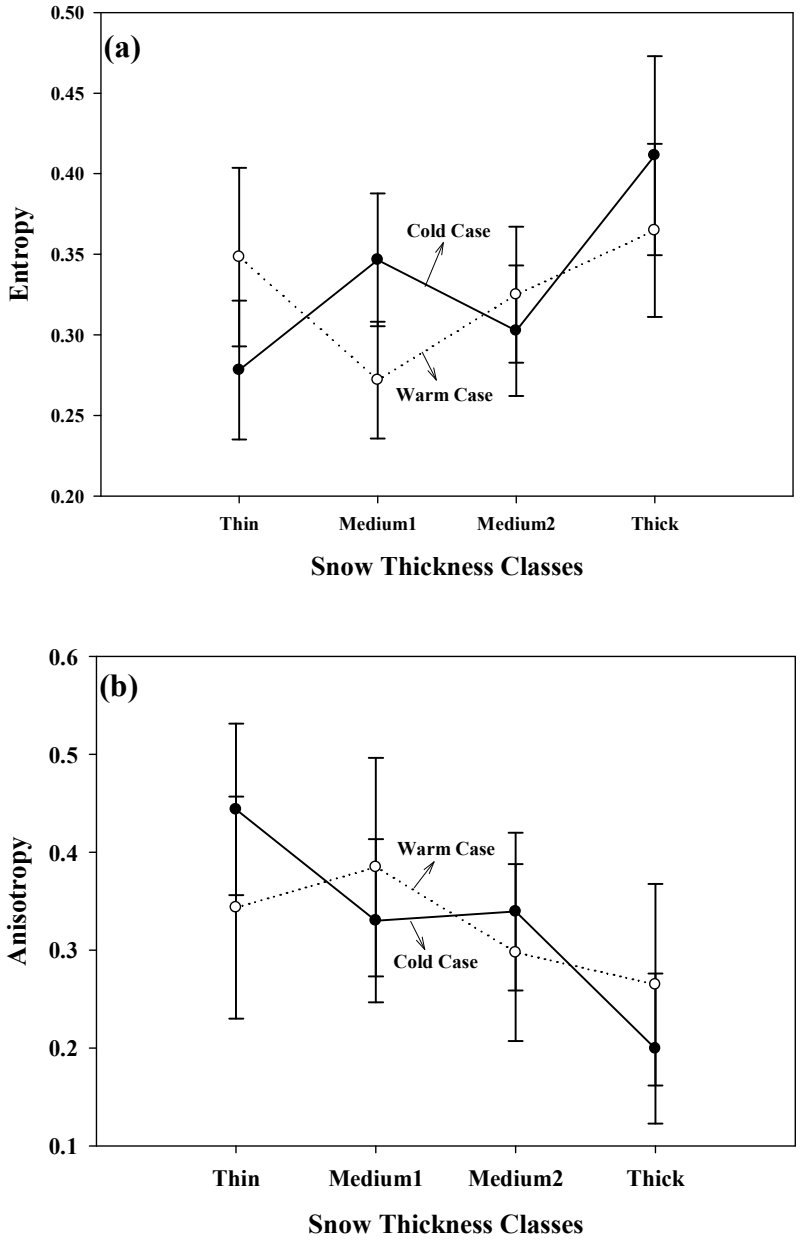

Figure 5.4: Polarimetric target decomposition parameters measured over snow covered SFYI at two different surface air temperatures (cold and warm). X-axis contains snow thickness classes and Y-axis represents (a) Entropy, and (b) Anisotropy. The solid and dotted points represent the mean sample values at -8.0°C (cold case) and -0.4°C (warm case) climatic regimes respectively. The error bars represent the standard deviation of each class.

Anisotropy (A) indicating the presence of multiple scattering (Cloude and Papathanassiou, 1999) is highest for thin snow and it decreases with increasing snow thickness except for medium1 for both cases (Figure 5.4b). The higher value of A is observed for the thin class for the cold climatic regime compared to the warm case.

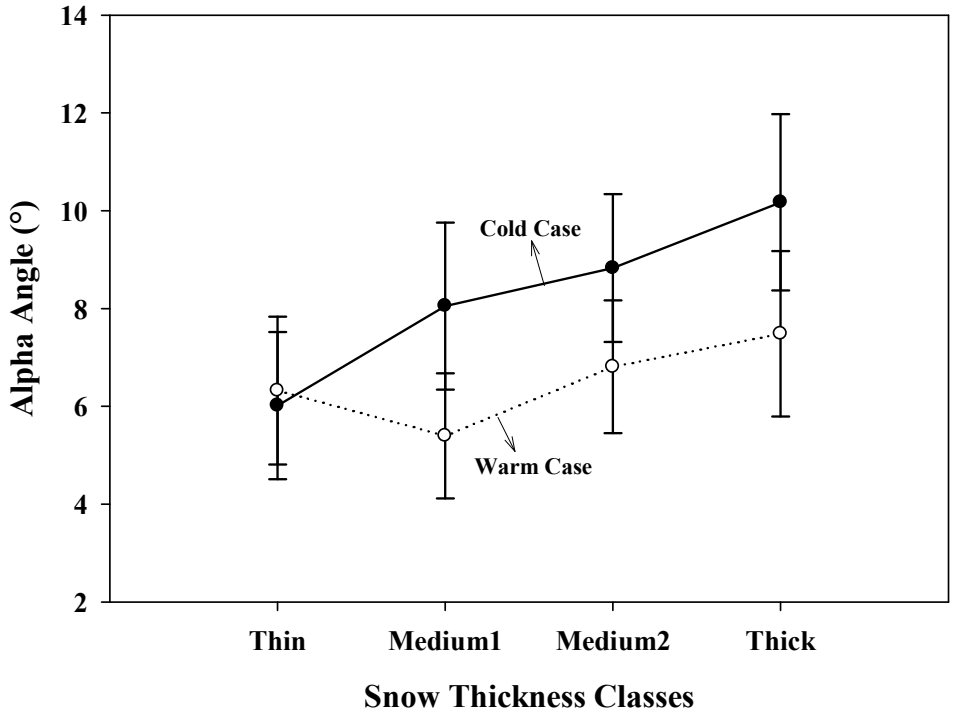

Figure 5.5: Polarimetric target decomposition parameters measured over snow covered SFYI at two different surface air temperatures (cold and warm). X-axis contains snow thickness classes and Y-axis represents Alpha Angle. The solid and dotted points represent the mean sample values at -8.0°C (cold case) and -0.4°C (warm case) climatic regimes respectively. The error bars represent the standard deviation of each class.

Alpha angle (α) identifies the dominant scattering mechanism available in the object material. A lower magnitude of α indicates dominant surface scattering, a moderate magnitude represents dominant volume scattering and the higher value indicates the presence of double-bounce scattering (Cloude and Pottier, 1997). A similar result is evaluated in the previous section

5.2. The higher magnitude of α observed for thicker snow cover for both cases and lower α for thin and medium1 snow covers for the cold and warm cases, respectively (Figure 5.5) indicate that the number of important scattering mechanisms increases with increasing snow thickness.

5.4 Proportional Contribution of the Three-Component Scattering Model

The proportional contributions of scattering from the three-component scattering model from different snow thickness classes over SFYI for two climatic regimes are presented in Table 5.3. Surface scattering (P_s) plays a dominant role for all classes under the two climatic regimes. The higher value of P_s is observed for thin and medium1 snow classes according to the cold and warm cases. This result can be due to P_s scattering contributed from ice surface for the cold case where dry snow acts as though it were transparent to microwave radiation. In warm cases higher variability of snow cover can produce a higher magnitude of surface scattering from the medium1 class. The lower proportion of surface scattering is observed for thick snow cover for both cases (Cold and Warm), indicating that the microwave energy is in less contact with enlarged and brine coated basal layer snow grains. It also exhibits higher magnitude of P_s for the warm case compared to the cold case for all snow classes except for thin (Table 5.3). This can be due to a thermodynamic effect of SWE whereby the dry thin snow cover allows 5.3 GHz microwaves to pass through both the snow and upper few centimeters such that surface scattering remains nearly the same as at the ice surface. The higher variation of the proportional contribution of surface scattering (8.65%) is observed for the thick snow classes compared to other snow classes for both climate regimes. This can again be the result of a wet snow cover, larger snow grain size, higher snow density and a higher volume of brine. The proportional contribution of volume scattering (P_v) increases with increasing snow thickness for cold cases

except for the medium2 class due to the low internal variability of snow properties (lower standard deviation). For the warm case, volume scattering decreases with increasing snow thickness until the medium1 class, then it slightly increases with thick snow (Table 5.3). The significant inter-class variability of P_v observed for the clod case compared to the warm case can be due to a dry snow-ice surface, snow grains and heterogeneous snow density.

Table 5.3: The proportional contribution of the three-component scattering model over snow covered SFYI at two climatic regimes.

	Snow Sites	P_s **(%)**	P_d **(%)**	P_v **(%)**	**Total**
Cold	Thin	88.17	3.36	8.47	100
	Medium1	82.84	3.43	13.73	100
	Medium2	85.19	3.53	11.28	100
	Thick	75.55	2.04	22.41	100
Warm	Thin	86.00	1.83	12.17	100
	Medium1	90.07	1.75	8.172	100
	Medium2	86.96	1.67	11.37	100
	Thick	84.50	1.50	14.00	100

P_v becomes higher for thin and thick snow classes for both cases and P_v increases for the thin class for the warm condition and decreases for the thick class for warm conditions. This can be due to a thermodynamic effect of SWE whereby the thinnest snow permitted the largest amount of temperature change at the snow-ice interface and this resulted in a subsequent increase in basal snow grain size and/or brine volume increase and brine coating of these enlarged grains. As previously mentioned, these brine-wetted depth hoar snow grains increase the dielectric permittivity at this interface thereby causing a larger increase in volume scattering compared to thicker snow cover situations. The proportional contribution of P_d to the total scattering exhibits low magnitude for both cases and shows significant relation with snow thickness. P_d increases

with increasing snow thickness for cold cases except for the thickest snow class and it decreases with increasing snow thickness for warm cases (Table 5.3).

5.5 Summary

Section 5.0 has described the results and analysis of the significance of polarimetric parameters at various snow cover distribution over smooth FYI. Section 5.1 has presented the results of absolute contribution of three-component scattering mechanisms on various snow classes over SFYI at two different climatic regimes. The results indicate that higher signature measured at warmer climatic regimes compared to colder cases except for thick snow class at volume scattering signature. These differences are evident in the cross-polarization backscatter signature in the section 5.2. These variations can be due to previous days SAT effect of cold climatic cases as well as low temperature gradient over thicker snow cover compared to thin snow classes. Section 5.3 has described the results of polarimetric target decomposition signatures on various snow classes over SFYI at two different climatic regimes. The results indicate that alpha angle has less sensitivity with SAT effect on thin snow classes which can be useful for snow cover discrimination at different climatic conditions. Section 5.4 has presented the results of proportional contribution of three-component scattering mechanisms over four various snow classes. The results indicate that P_s decreases with snow thickness at cold cases and increases with snow thickness at warm cases for most of the snow classes. It also indicates that P_v increases with snow thickness at cold cases and decreases with snow thickness at warm cases for most of snow classes. The results also show higher variation observed at thick snow classes compared to other snow classes.

Chapter Six

CONCLUSIONS AND FUTURE WORK

6.0 Conclusions

6.1 Influences of Incidence Angle Variations for FYI Type Discrimination

In this study, a three-component scattering model (Freeman and Durden, 1998) is used to discriminate three types of snow covered first-year sea ice (smooth ice-SI, rough ice-RI and deformed ice-DI). Results from this analysis show that decomposition of the total scattering power can identify three separate scattering processes: surface (P_s), volume (P_v), and double-bounce (P_v). It is observed that a steeper incidence angle (i.e. 29°) provided better discrimination of different FYI types than a shallower angle (39°). It is also observed that surface and volume scattering play a dominant role for all three first-year ice types, and double-bounce scattering makes very little contribution to the total amount of scattering. The study also measures the effects of radar incidence angle ranges on the three scattering processes and highlights a subtle effect of increased volume scattering (P_v) for smooth FYI at a shallower incidence angle compared to a steeper one. It is speculated that enlarged, brine coated, high dielectric basal layer snow grains are the reason for the observed difference. Future work will extend the methodological approach to evaluate the effect of temperature and snow thickness over landfast first-year sea ice using this three-component scattering model.

6.2 Snow Cover Distributions over Smooth FYI

In this study, a three-component scattering model (Freeman and Durden, 1998) is used to discriminate four different snow thickness classes ranging from 8 to 36 cm in mean thickness over smooth first-year sea ice. Results from this analysis show that decomposition of the total scattering power can identify three separate scattering processes: surface (P_s), volume (P_v), and double-bounce (P_d). It is observed that surface and volume scattering plays a dominant role for all four snow thickness classes, and double-bounce scattering has very little impact on the total amount of scattering. The analysis provides measures of the effects of air temperature forced snow surface and snow-ice interface temperatures on the three scattering processes and highlights a subtle effect of larger amounts of scattering for air and snow temperature regimes approaching 0^{o}C for all snow thickness classes compared to cold climatic regimes ($\sim -8.0° \, C$). The results also show that for a given change in snow surface or air temperature, larger variation in polarimetric synthetic aperture radar (POLSAR) measures is observed for thin and medium snow thicknesses compared to the thickest snow cover.

The results from a cold-warm image difference exhibited a relatively small change (1.5 dB 1.53 dB) in absolute value of P_s for thick snow cover and larger change ($> \, 6 \, dB$) for both thin and medium snow cover. Changes in P_v scattering is for thin ($> \, 8 \, dB$), medium1 ($> \, 5 \, dB$), medium2 ($> \, 8 \, dB$) and lower for thick ($< \, 1 \, dB$) snow cover.

6.3 Future work

These results help advance our understanding towards development of an "Electro-Thermo-Physical" model for snow-covered FYI (Barber et al., 1998a; Barber and Nghiem, 1999) which would allow us to assess numerous climatic variables of snow covered sea-ice (e.g., ice-surface temperature, spatio-temporal estimates of SWE, snow melt onset, and snow surface albedo, etc.) from spaceborne polarimetric SAR observations.

Future work will exploit this theory to test the range of geophysical and thermodynamic conditions under which such a SAR-SWE relationship may exist through the use of both spaceborne and surface-based polarimetric SAR data. The penultimate goal of these in situ process studies is "up-scaling" to provide regional and hemispheric-scale estimates of these surface and climate state variables using time-series microwave data.

BIBLIOGRAPHY

Barber, D.G., & Nghiem, S.V. (1999). The role of snow on the thermal dependence microwave ice. *Journal of Geophysical Research,*l.104, C11, .25789-25803.

Barber, D.G., Yackel, J.J., and Hanesiak, J.M. (1999). Sea ice decay for marine navigation. *Final Report submitted to the University of Manitoba,* Center for Earth Observation Science, Winnipeg, MB, Canada, CEOSTEC-10-1-99.

Barber, D. G., Fung, A. K., Grenfell, T. C., Nghiem, S. V., Onstott, R. G., Lytle, V. I., Perovich, D. K., & Gow, A. J. (1998a). The role of snow on microwave emission and scattering over first-year sea ice. *IEEE Trans. Geosci. Rem. Sens.*, 36,5, 1750-1763.

Barber, D.G., Yackel, J.J., Wolfe, R.L., & Lumsden, W. (1998b). Estimating the thermodynamic state of snow covered sea ice using time series synthetic aperture radar (SAR) data. *Proceedings of the Eighth International Offshore and Polar Engineering Conference, Montreal, Canada, May 24-29.*

Barber, D.G., & Thomas, A. (1998). The influence of cloud cover on the radiation budget, physical properties, and microwave scattering coefficient (σ°) of first-year and multiyear sea ice. *IEEE Transactions on Geoscience and Remote Sensing,* 36:1, 38-50.

Barber, D.G., & LeDrew, R. (1995). Statistical analysis of the geophysical and electrical properties of snow on landfast first-year sea ice. *Journal of Geophysical Research,* 100:C2, 2673-2686.

Barber, D.G., Papakyriakou, T.N., LeDrew, E.F., & Shokr, M.E. (1995). An examination of the relation between the spring period evolution of the scattering coefficient (σ) and radiative fluxes over landfast sea-ice. *International Journal of Remote Sensing, 16:17,*3343-3363.

Barber, D.G., & LeDrew, E.F. (1991). SAR sea ice discrimination using texture statistics: A multivariate approach. *Photogrammetric Engineering & Remote Sensing, 57:4, 385-395.*

Beaven, S.G., Lockhart, G.L., Gogineni, S. P., Hossetnmostafa, A.R., Jezek, K., Gow, A.J., Perovich, D.K., Fung, A.K., & Tjuatja, S. (1995). Laboratory measurements of radar backscatter from bare and snow-covered saline ice sheets. *International Journal of Remote Sensing,* 16:5, 851-876.

Bredow, J.W., & Gogineni, S. (1990). Comparison of measurements and theory for backscatter from bare and snow-covered saline ice. *IEEE Transactions on Geoscience and Remote Sensing,* 28:4, 456-463.

Carlström, A., & Ulander, L. M. H. (1995). Validation of backscatter models for level and deformed ice sea ice in ERS-1 SAR images. *International Journal of Remote Sensing,* 16:7, 3245-3266.

Budikova, D. (2009). Role of Arctic sea ice in global atmospheric circulation: A review. *Global and Planetary Change,* 68, 149-163.

Carmack, E.C. (1986). Circulation and mixing in ice-covered waters. In: N. Untersteiner (Ed.), The geophysics of sea ice, (pp. 641-712). Plenum, New York.

Cloude, S.R., & Pottier, E. (1996). A review of target decomposition theorems in radar polarimetry. *IEEE Transactions on Geoscience and Remote Sensing,*34:2, 498-518.

Cloude, S.R., & Pottier, E. (1997). An entropy based classification scheme for land applications of polarimetric SAR. *IEEE Transactions on Geoscience Remote Sensing*, 35:1, 68-78.

Cloude, S.R., & Papathanassiou, K.P. (1999). Surface roughness and polarimetric entropy. *In proceeding.IGARSS.* Humburg.Germany, 2443-2445.

Colbeck, S.C. (1982). An overview of seasonal snow metamorphism. *Reviews of Geophysics and Space Physics, 20:1,* 45-61.

Colbeck, S.C (1983). Theory of metamorphism of dry snow. *Journal of Geophysical Research,* 88:C9, 5475-5482.

Comiso, J.C. (1995). Satellite remote sensing of the Arctic Ocean and Adjacent seas. In *Arctic Oceanography:Marginal Ice Zones and Continental Shelves, Coastal Estuarine Stud.,*49, edited by W.O. Smith Jr. & J.M. Grebmeir, 1-50, AGU, Washington, D.C.

Cox, G.F.N., & Weeks, W.F. (1983). Equations for determining the gas and brine volumes in sea-ice samples. *Journal of Glaciology,* 29:12, 306-316.

Cox, G.F.N., & Weeks, W.F. (1974). Salinity variations in sea ice. *Journal of Glaciology,* 13:67, 109-120.

D'Alvise, R., Moloney, C., & Ramponi, G. (1999). Statistical methods for the evaluation of the coefficient of variation in SAR images. *Processings of IGARSS,2, 1253-1255.*

Dabboor, M., Yackel, J.J., Hossain, M.M., & Burn, A. (2012). Comparing matrix distance measures for unsupervised polarimetric SAR data classification of sea ice based on agglomerative clustering. *International Journal of Remote Sensing.(*Accepted)

Dierking, W. (2010). Mapping of different sea ice regimes using images from Sentinel-1 and ALOS synthetic aperture radar. *IEEE Transactions on Geoscience and Remote Sensing,* 48:3, 1045-1058.

Dierking, W., & Dall, J. (2007). Sea-ice deformation state from synthetic aperture radar imagery-part I: comparison of C- and L-band and different polarization. *IEEE Transactions on Geoscience and Remote Sensing,* 45:11, 3610-3622.

Dierking, W., & Askne, J. (1998). Polarimetric L- and C-band SAR signatures of Baltic Sea ice observed during EMAC-95. *Proc. 17th EARSel Symposium,* Lyngby, Denmark. 329-336.

Drobot, S.D., & Anderson, M.R. (1998). An improved method for determining snowmelt onset dates over Arctic sea ice using scanning multichannel microwave radiometer and Special Sensor Microwave/Imager data. *Journal of Geophysical Research, 106:D20,* 24033-24049.

Drinkwater, M.R., & Kwok, R. (1991). Stokes matrix statistics in sea ice polarimetric SAR images, *Proceedings of the IGARSS'91Symposium*. Vol.1.pp.99-102. IEEE catalog no.91 CH2971-0, IEEE, New York.

Drinkwater, M.R., Kwok, R., Winebrenner, D.P., & Rignot, E. (1991). Multifrequency Polarimetric Synthetic Aperture Radar Observations of Sea Ice. *Journal of Geophysical Research,* 96:C11, 20679-20698.

Drinkwater, M.R., Kwok, R., Rignot, E., Iseaelsson, H., Onstott, R. G., & Winebrenner, D.P. (1992). Potential Applications of Polarimetry Classification of Sea Ice. *Microwave Remote Sensing of Sea Ice. F. Carsey ed.* Washington D.C.: AGU. 419-430.

Durden, S. L., Van Zyl, J.J., & Zebker, H.A. (1989). Modeling and observations of the radar polarization signatures of forested areas. *IEEE Transactions on Geoscience and Remote Sensing,* 27:3, 290-301.

Eicken, H. (2003). Chapter 2: From the microscopic to the macroscopic to the regional scale: Growth, microstructure and properties of sea ice. In *Sea Ice: An Introduction to its Physics, Biology, Chemistry and Geology,* Thomas, D.N., Dieckman, G.S., (eds). Blackwell Scientific Ltd.: London, 22-81.

Eicken, H., Fischer, H., Lemke, P. (1995). Effects of the snow cover on Antarctic sea ice and potential modulation of its response to climate change. *Annals of Glaciology,* 21, 369-376.

Eicken, H. (1992). Salinity profiles of Antarctic sea ice: Field data and model results. *Journal of Geophysical Research,* 97:C10, 15545-15557.

Evans, D.L., Farr, T.G., Van Zyl, J.J., & Zebker, H.A. (1988). Radar Polarimetry: Analysis Tools and Applications. *IEEE Transactions on Geoscience and Remote Sensing,* 26:6, 774-789.

Ferguson, S., Stirling, I., McLoughlin, P. (2005). Climate change and ringed seal (*Phoca hispida*) recruitment in western Hudson Bay. *Marine Mammal Science,* 21, 121-135.

Freeman, A. (1992). SAR Calibration: An Overview. *IEEE Transactions on Geoscience and Remote Sensing,* 30:6, 1107-1121.

Freeman, A., & Durden, S. (1992). A three-component scattering model to describe Polarimetric SAR data. *In Proc. SPIE Conference Radar Polarimetry.* San Diego, CA, July. 213-224.

Freeman, A., & Durden, S. (1998). A three-component scattering model for Polarimetric SAR data. *IEEE Transactions on Geoscience and Remote Sensing,* 36:3, 963-973.

Frost, K.J., Lowry, L.F., Gilbert, J.R., & Bums, J.J. (1988). Ringed seal monitoring: relationships of distributin and abundance to habitat attributes and industrial activities. *Unpublished final report RU No. 667 to Outer Continental Shelf Environmental Assessment Program.* Anchorage, AK.

Furgal, C.M., Innes, S., & Kovacs, K.M. (1996). Characteristics of ringed seal, *Phoca hipida,* subnivian structures and breeding habitat and their effects on predation. *Canadian Journal of Zoology,*74, 858-874.

Fung, A.K. (1994). Microwave scattering and emission models and their applications. *Artech.* House. Norwood.USA.

Geldsetzer, T., Yackel, J.J. (2009). Sea ice type and open water discrimination using dual co-polarized C-band SAR. *Canadian Journal of Remote Sensing*, 35:1,73-84.

Geldsetzer, T., Mead, J.B., Yackel, J.J., Scharien, R.K., & Howell, S.E.L. (2007). Surface-based polarimetric C-band scatterometer for field measurements of sea ice. *IEEE Transactions on Geoscience and Remote Sensing,* 45:11, 3405-3416.

Gough, W.A., Cornwell, A.R., & Tsuji, L.J.S. (2004). Trends in seasonal sea duration in southwestern Hudson Bay. *Arctic,* 57:3, 299-305.

Hanesiak, J., Barber, D.G., & Flato, G. (1999). Role of diurnal processes in the seasonal evolution of sea ice and its snow cover. *Journal of Geophysical Research,* 104:C6. doi:10.1029/1999JC900054.

Howell, S.E.L., Yackel, J.J., De Abreu, R.A., Geldsetzer, T., & Breneman, C. (2005). On the utility of SeaWinds/QuickSCAT for the estimation of the thermodynamic state of first-year sea ice. *IEEE Transactions on Geoscience and Remote Sensing,* 43:6, 1338-1350.

Iacozza, J., & Barber, D.G. (2010). An examination of snow redistribution over smooth land-fast sea ice. *Hydrological Process,* 24, 850-865.

Iacozza, J., & Barber, D.G. (2001). Ablation patterns of snow cover over smooth first-year sea ice in the Canadian Arctic. *Hydrological Processes,* 15, 3559-3569.

Iacozza, J., & Barber, D.G. (1999). An examination of the distribution of snow on sea ice. *Atmosphere-Ocean,* 37:1, 21-51.

IPCC (International Panel on Climate Change). (1996). *Climate Change*: *The IPCC Assessment.* J.T. Houghton, G.J. Jenkens and J.J. Ephraums (Eds), Cambridge University Press, Cambridge,

U.K., 365 pp.

Karvonen, J., Simila, M., & Heiler, I. (2003). Ice thickness estimation using SAR data and ice thickness history. *Proc. IGARSS'03*, Toulouse, France, CD I: 74-76.

Kinnard, C., Zdanowicz, C.M., Fisher, D.A., Isaksson, E., de Vernal, A., & Thompson, L.G. (2011). Reconstructed changes in Arctic sea ice over the past 1450 years. *Nature,* 479, 509-512.

Klein, L.A., & Swift,C. (1977). An improved model for the dielectric constant of seawater at microwave frequencies. *IEEE Transactions Antennas Propagations,* AP-25:1, 104-111.

Kotlyakov, V.M., & Grosswald, M.G. (1990). Interaction of sea ice, snow and glaciers with the atmosphere and ocean. *Polar Geog Geol.,* 14:1, 3-248.

LeDrew, E.F. (1986). Sensitivity of the Arctic Climate: A factor in Developing Planning Strategies for Our Arctic Heritage. *Environmental Conservation,* 13, 215-228.

Lee, J., Ainsworth, T.L., Kelly, J.P., & Lopez-Martinez, C. (2008). Evaluation and bias removal of multilook effect on entropy/alpha/anisotropy in polarimetric SAR decomposition. *IEEE Transactions on Geoscience and Remote Sensing,* 46:10, 3039-3052.

Lee, J.S., Cloude, S.R., Papathanassiou, K., Grunes, M.R., Ainsworth, T.L., & Schuler, D.L. (2002). Speckle filtering of polarimetric SAR interferometry data. *Geoscience and Remote Sensing Symposium,IGARSS'02, June 24-28,* 6, 832-834.

Livingstone, C.E., & Drinkwater, M.R. (1991). Springtime C-band SAR backscatter signatures of Labrador sea marginal ice: measurements versus modeling predictions. *IEEE Transactions on Geoscience and Remote Sensing,* 29, 29-41.

Livingstone, C.E., Onstott, R.G., Arsenault, L.D., Gray, A.L., & Singh, K.P. (1987). Microwave sea-ice signature near the onset of melt. *IEEE Transactions on Geoscience and Remote Sensing,* GE-25:2, 174-187.

Lundhaug, M. (2002). ERS SAR studies of sea ice signatures in the Pechora Sea and Kara Sea region. *Canadian Journal of Remote Sensing,* 28:2, 114-127.

Lytle, V.I., Jezek, K.C., Hosseinmostafa, A.R., & Gogineni, S.P. (1993). Laboratory backscatter measurements over urea ice with a snow cover at Ku band. *IEEE Transactions on Geoscience and Remote Sensing,*31:5, 1009-1016.

Manninen, A.T. (1992). Effect of ice properties on calculated surface backscattering in BEPERS-88. *International Journal of Remote Sensing,* 13:13, 2469-2487.

Markus, T., & Cavalieri, D.J. (1998). Snow depth distribution over sea ice in the Southern Ocean from satellite passive microwave data, Antarctic Sea Ice: Physical Processes, Interactions and Variability. *Antarctic Research Series,* 74, 19-39.

Martin, S., Yu, Y., & Drucker, R. (1996). The temperature dependence of frost flower growth on laboratory sea ice and the effect of the flowers on infrared observations of the surface. *Journal of Geophysical Research,* 101:C5, 12111-12125.

Maslanik, J., Stroeve, J., Fowler, C., & Emery, W. (2011). Distribution and trends in Arctic sea ice age through spring 2011. *Geophysical Research Letters,* 38, L13502, doi: 10.1029/2011GL047735.

Maykut, G.A. (1986). The surface heat and mass balance. In: Untersteiner, N. (ed.) *The Geophysics of Sea Ice. Dordrecht:*Martinus Nijhoff Publ. pp.395-463.

Maykut, G.A. (1978). Energy exchange over young sea ice in the central Arctic. *Journal of Geophysical Research,* 83:C7, 3646-3658.

Mellor, M. (1977). Engineering properties of snow. *Journal of Glaciology,* 19:81, 15-66.

Moritz, R.E., & Perovich, D.K. (1996). Surface Heat Budget of the Arctic Ocean Science Plan. *ARCHSS/OAII report number 5.* University of Washington, Seattle, p.64.

Monaghan, A., & Bromwich, D. (2008). Climate science: Global warming at the poles. *Nature Geoscience,*1, 728-729.

MSC (Meteorological Service of Canada). (2005). Manual of standard procedures for observing and reporting ice conditions, revised ninth edition. *Environment Canada, Ottawa.*

Nakawo, M., & Sinha, N.K. (1981). Growth rate and salinity profile of first-year sea ice in the high Arctic. *Journal of Glaciology,* 27:96, 315-330.

Nghiem, S. V., Kwok, R., Yueh, S. H., Gow, A. J., Perovich, D. K., Kong, J. A., Hsu, C. C. (1997). Evolution in polarimetric signatures of thin saline ice under constant growth. *Radio Science*. 32:1, 127 – 151.

Nghiem, S.V., Kwok, R., Yueh, S.H., & Drinkwater, M.R. (1995). Polarimetric signatures of sea ice 2: Experimental model. *Journal of Geophysical Research,* 100:C7, 13681-13698.

Ono, N., & Kasai, T. (1985). Surface layer salinity of young sea ice. *Annals Glaciology,* 6, 298-299.

Petrich, C., Eicken, H., Polashenski, C.M., Sturm, M., Harbeck, J.P., Perovich, D. K., & Finnegan, D.C. (2012). Snow dunes: a controlling factor of melt pond distribution on Arctic sea ice. (*In-review*)

Scheuchl, B., Hajnsek, I., & Cumming, I. (2002). Model-based classification of Polarimetric SAR sea ice data. *Proc. IGARSS'02.* Toronto. June.

Scheuchl, B., Cumming, I., & Hajnsek, I. (2005). Classification of fully polarimetric single- and dual-frequency SAR data of sea ice using the Wishart statistics. *Canadian Journal of Remote Sensing,* 31:1, 61-72.

Schwerdtfeger, P. (1963). The thermal properties of sea ice. *Journal of Glaciology,* 4:36, 789-807.

Serreze, M.C., Barrett, A.P., Stroeve, J.C., Kindig, D.N., & Holland, M.M. (2009). The emergence of surface-based Arctic amplification. *The Cryosphere,*3, 11-19.

Simila, M., Karvonen, J., Haas, C., & Hallikainen, M. (2006). C-band SAR based estimation of Baltic Sea ice thickness distributions. *Proc. Geoscience and Remote Sensing, IGARSS'06*, 710-713.

Stirling, I., & Smith, T.G. (2004). Implications of warm temperatures and unusual rain events for the survival of ringed seals on the coast of southeastern Baffin Island. *Arctic,* 57, 59-67.

Stirling, I., Andriashek, D., & Calvert, W. (1993). Habitat preferences of polar bears in the western Canadian Arctic in late winter and spring. *Polar Record,* 29, 13-24.

Stogryn, A., & Desargant, G.J. (1985). The dielectric properties of brine in sea ice at microwave frequencies. *IEEE Transactions Antennas Propagation, AP-33:5,* 523-532.

Sturm, M., Maslanik, J.A., Perovich, D.K., Stroeve, J.C., Richter-Menge, J., Markus, T., Holmgren, J., Heinrichs, J.F., & Tape, K. (2006). Snow Depth and Ice Thickness Measurements From the Beaufort and Chukchi Seas Collected During the AMSR-Ice03 Campaign. *IEEE Transactions on Geoscience and Remote Sensing,* 44:11, 3009-3020.

Sturm, M., Holmgren, J., Perovich, D.K. (2002). The winter snow cover on the sea ice of the Arctic Ocean at the Surface Heat Budget of the Arctic Ocean (SHEBA): temporal evolution and spatial variability. *Journal of Geophysical Research,* 107:C10, 8047.

Swift, T, C. (1999). Seasat Scatterometer Observations of Sea Ice. *IEEE Transactions on Geoscience and Remote Sensing,* 37:2, 716-723.

Thomsen, B.B., Nghiem, S.V., & Kwok, R. (1998). Polarimetric C-band SAR observations of sea ice in the Greenland Sea. *Proceedings of the IGARSS '98 Symposium,* Seattle, WA.

Tivy, A., Howell, S. E. L., Alt, B., Mccourt, S., Chagnon, R., Crocker, G., Carrieres, T., & Yackel, J. J. (2011). Trends and variability in summer sea ice cover in the Canadian Arctic based on the Canadian Ice Service Digital Archive, 1960–2008 and 1968–2008, *Journal of . Geophysical Research,* 116, C03007, doi:10.1029/2009JC005855.

Tjuatja, S., Fund, A.K., & Comiso, J.C. (1995). Effects of snow cover on sea ice emission. In *Proceedings of the International Geoscience and Remote Sensing Symposium (IGARSS'95), 10-14 July, Florence, Italy,* 697-699.

Topouzelis, K., Karathanassi, V., Pavlakis, P. & Rokos, D. (2008). Dark formation detection using neural networks. *International Journal of Remote Sensing*, 29, 4705–4720.

Touzi, R., Goze, S., Toan, T.L., Lopes, A., & Mougin, E. (2002). Polarimetric discriminators for SAR images. *IEEE Transactions on Geoscience and Remote Sensing,* 30:5, 973-980.

Touzi, R. (2007). Target Scattering Decomposition in Terms of Roll-Invariant Target Parameters. *IEEE Transactions on Geoscience and Remote Sensing,* 45:1, 73-84.

Tucker III, W.B., Perovich, D.K., Gow, A.J., Weeks, W.F., & Drinkwater, M.R. (1992). Physical properties of sea ice relevant to remote sensing, in *Microwave Remote Sensing of Sea Ice, Geophysical Monograph 68,* edited by F.Carsey, 9-26, AGU, Washington, D.C.

Tiuri, M.E., Sihvola, A.H., Nyfors, E.G., & Hallikainen, M.T. (1984). The complex dielectric constant of snow at microwave frequencies. *IEEE Journal of Ocean Engineering, OE-9:5,* 377-382.

Ulaby, F.T., Sarabandi, K., Mcdonald, K.C., Whitt, M., & Dobson, M.C. (1990). Michigan Microwave Canopy Scattering Model (MIMICS). *International Journal of Remote Sensing,* 11, 1223-1253.

Ulaby, F.T., & Elachi, C. (*editors).* (1990). Radar Polarimetry for Geoscience Applications. *Mass: Artech House.*

van Der Sanden, J.J. (2004). Anticipated applications potential of RADARSAT-2 data. *Canadian Journal of Remote Sensing,* 30:3, 369-379.

Van Zyl, J. J. (1989). Unsupervised classification of scattering behavior using radar Polarimetry data. *IEEE Transactions on Geoscience and Remote Sensing.* GE-27. 3645.

Wadhams, P. (2000). *Ice in the Ocean*, Overseas Publishers Association, Amsterdam.

Wang, J.R., Chang, A.T.C., & Sharma, A.K. (1992). On the estimation of snow depth from microwave radiometric measurements. *IEEE Transactions on Geoscience and Remote Sensing,* 30:4, 785-792.

Walter, K. M., Melanie, E., Claude, R. D., Martin, O. J., & Chapin, F.S. III. (2008). The Potential Use of Synthetic Aperture Radar for Estimating Methane Ebullition From Arctic Lakes. *Journal of the American Water Resources Association (JAWRA)*, 44:2, 305-315. DOI: 10.1111/j.1752-1688.2007.00163.x

Wang, J., Mysak, L.A., & Ingram, R.G. (1994). Inter annual variability of sea-ice cover in Hudson Bay, Baffin Bay and the Labrador Sea. *Atmosphere-Ocean,* 32:2, 421-447.

Weeks, W.F., & Ackley, S.F. (1982). The growth, structure, and properties of sea ice, *Cold Regions Research and Engineering Lab,* Hanover Nh.

Wen, T., Felton, W.J., Luby, J.C., Fox, W.L.J., & Kientz, K.L. (1989). Environmental measurements in the Beaufort Sea, Spring 1988. *Technical Report APL-UW TR 822*, Appl. Phys. Lab., University of Washington, Seattle.

Wettlaufer, J.S., & Worster, M.G. (1995). Dynamics of premelted films: Frost heave in a capillary. *Physical Review,* E51:5, 4679-4689.

Winebrenner, D. P., Farmer, L. D., & Joughin, I. R. (1995). On the response of polarimetric synthetic aperture radar signatures at 24 cm wavelength to sea ice thickness in Arctic leads. *Radio Science*, 30: 2, 373-402.

WMO (World Meteorological Organization). (2007). WMO sea ice nomenclature. WMO-No.259 Suplement No.5. pp23.

Yackel, J.J., Barber, D.G., Papakyriakou, T.N., & Breneman, C. (2007). First-year sea ice spring melt transitions in the Canadian Arctic Archipelago from time-series synthetic aperture radar data, 1992-2002. *Hydrological Processes,*21, 253-265.

Yackel, J.J., Barber, D.G. (2007). Observations of snow water equivalent change on landfast first-year sea ice in winter using synthetic aperture radar data. *IEEE Transactions on Geoscience and Remote Sensing,* 45:4, 1005-1015.

Zebker, H., & Van Zyl, J.J. (1991). Imaging radar polarimetry: A review, *Proceedings of the IEEE,* 79:11, 1583-1606.

Appendix-A

Table A-1: Results of C-band POLSAR signatures of landfast FYI types at two different radar incidence angles

POLSAR Parameters	**FYI Types**	**POLSAR Signatures (Means and Standard Deviations)**			
		(28.06-29.82)°		**(38.38-39.85)°**	
		Mean	Std	Mean	Std
σ_{xx}^0	SI	-13.63	0.494	-14.99	1.15
	RI	-9.89	0.500	-11.56	0.79
	DI	-7.58	0.926	-9.29	0.83
σ_{yy}^0	SI	-13.79	0.696	-15.42	0.75
	RI	-9.96	0.505	-12.65	0.59
	DI	-7.53	0.909	-10.05	0.87
σ_{xy}^0	SI	-26.32	0.902	-25.66	1.31
	RI	-20.46	0.472	-21.40	0.96
	DI	-17.40	1.023	-18.29	0.82
γ_{co}	SI	0.1581	0.528	0.42	0.74
	RI	0.061	0.538	1.09	0.71
	DI	-0.052	0.519	0.75	0.58
γ_{cr}	SI	12.68	0.991	11.01	1.23
	RI	10.56	0.797	9.84	0.96
	DI	09.82	1.155	8.99	1.08
P_s	SI	-11.64	0.668	-13.57	0.94
	RI	-8.39	0.645	-11.12	0.85
	DI	-6.33	1.222	-9.35	1.55
P_v	SI	-17.71	1.009	-17.48	1.68
	RI	-11.50	0.500	-12.60	0.98
	DI	-8.46	1.005	-9.29	0.77
P_d	SI	-24.93	1.914	-28.51	6.88
	RI	-23.90	2.366	-25.29	5.72
	DI	-22.48	3.167	-24.31	7.25
P_s (%)	SI	77.27		69.48	
	RI	65.97		57.13	
	DI	61.09		48.89	
P_v (%)	SI	19.09		28.29	
	RI	32.18		40.68	
	DI	37.43		49.54	

P_d (%)	SI	3.63		2.23	
	RI	1.85		2.19	
	DI	1.48		1.56	
$SPAN$	SI	-10.45	0.513	-11.80	0.90
	RI	-6.53	0.385	-8.56	0.61
	DI	-4.10	0.845	-6.06	0.72
H	SI	0.43	0.042	0.52	0.04
	RI	0.54	0.045	0.63	0.04
	DI	0.55	0.060	0.67	0.06
A	SI	0.32	0.062	0.27	0.13
	RI	0.14	0.044	0.21	0.07
	DI	0.18	0.053	0.21	0.09
α	SI	7.96	1.655	10.80	2.12
	RI	10.12	0.985	14.42	1.94
	DI	13.09	2.102	16.31	3.02
PDH	SI	0.01	0.001	0.006	0.001
	RI	0.02	0.002	0.015	0.002
	DI	0.03	0.006	0.028	0.005
$\emptyset_{\boldsymbol{hh-vv}}$	SI	6.32	4.615	7.75	4.12
	RI	4.74	4.261	3.85	8.15
	DI	7.37	8.876	13.57	9.03
γ_{var}	SI	0.05	0.012	0.07	0.02
	RI	0.08	0.014	0.091	0.017
	DI	0.08	0.017	0.099	0.02
F_p	SI	0.91	0.021	0.87	0.03
	RI	0.85	0.024	0.83	0.028
	DI	0.85	0.029	0.82	0.039

Appendix-B

Table B-1: Results of polarimetric SAR C-band signatures over landfast FY smooth sea ice at two different surface air temperatures.

POLSAR Parameters	Snow Classes	POLSAR Signatures (Means and Standard Deviations)			
		May 4th/ -8°C		May 14th/ -0.4°C	
		Mean	Std	Mean	Std
σ_{xx}^{0}	Thin	-19.29	1.07	-12.58	1.09
	Med1	-22.47	0.83	-15.03	0.83
	Med2	-22.83	0.85	-14.51	0.78
	Thick	-14.23	1.01	-13.04	0.92
σ_{yy}^{0}	Thin	-19.34	1.05	-12.51	1.02
	Med1	-22.83	0.77	-15.21	0.78
	Med2	-22.79	0.88	-14.67	0.75
	Thick	-14.22	0.95	-13.14	0.97
σ_{xy}^{0}	Thin	-34.21	0.73	-26.99	1.07
	Med1	-34.74	0.74	-31.16	0.85
	Med2	-35.68	0.67	-29.06	0.71
	Thick	-26.28	1.21	-27.18	0.85
γ_{co}	Thin	0.05	0.49	-0.07	0.48
	Med1	0.36	0.55	0.18	0.39
	Med2	-0.03	0.49	0.16	0.42
	Thick	-6.14e-3	0.62	0.09	0.49
γ_{cr}	Thin	14.92	1.18	14.41	1.29
	Med1	12.27	1.04	16.13	1.12
	Med2	12.85	1.05	14.54	1.03
	Thick	12.05	1.34	14.13	1.23
P_s	Thin	-16.78	1.13	-10.07	1.12
	Med1	-20.31	0.87	-12.48	0.84
	Med2	-20.39	0.93	-12.08	0.83
	Thick	-12.21	1.11	-10.68	1.04
P_v	Thin	-26.89	0.88	-18.59	1.22
	Med1	-28.10	0.77	-22.89	0.83
	Med2	-29.13	0.75	-20.89	0.70
	Thick	-17.53	1.25	-18.45	0.85
P_d	Thin	-31.07	1.63	-27.69	4.19
	Med1	-34.41	1.89	-30.14	2.84
	Med2	-34.43	1.76	-29.98	3.46
	Thick	-29.21	4.69	-29.63	4.96

P_s (%)	Thin	88.17		86.00	
	Med1	82.84		90.07	
	Med2	85.19		86.96	
	Thick	75.55		84.50	
P_v (%)	Thin	8.47		12.17	
	Med1	13.73		8.17	
	Med2	11.28		11.37	
	Thick	22.41		13.99	
P_d (%)	Thin	3.37		1.83	
	Med1	3.43		1.75	
	Med2	3.53		1.67	
	Thick	2.04		1.49	
$SPAN$	Thin	-16.16	1.00	-9.37	1.00
	Med1	-19.36	0.71	-11.99	0.76
	Med2	-19.57	0.78	-11.43	0.71
	Thick	-10.93	0.89	-9.90	0.87
H	Thin	0.28	0.04	0.35	0.06
	Med1	0.35	0.04	0.27	0.04
	Med2	0.30	0.04	0.32	0.04
	Thick	0.41	0.06	0.36	0.05
A	Thin	0.44	0.09	0.34	0.11
	Med1	0.329	0.08	0.38	0.11
	Med2	0.339	0.08	0.29	0.09
	Thick	0.199	0.08	0.26	0.10
α	Thin	6.02	1.50	6.32	1.51
	Med1	8.05	1.71	5.39	1.28
	Med2	8.83	1.51	6.81	1.36
	Thick	10.17	1.81	7.48	1.69
$\boldsymbol{P_s - P_v}$	Thin	10.12	1.27	8.52	1.44
	Med1	7.79	1.17	10.42	1.12
	Med2	8.75	1.21	8.82	1.11
	Thick	5.32	1.59	7.77	1.37